Highly durable fuel cell electrocatalyst with low-loading Pt-Co nanoparticles dispersed over single-atom Pt-Co-N-Graphene nanofiber

Supplementary Information

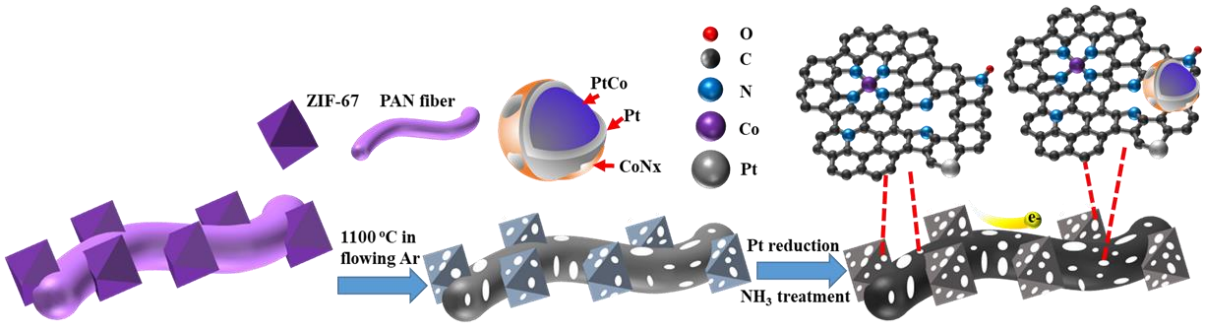

Supplementary Fig. 1| Schematic illustration for the synthesis of PtCo@Pt-Co-GNF with ammonolysis in pure NH_3 to form additional PGM-free active sites including Co-N_4, Pyridinic-N, as well as micropores, PtCo alloys, CoN/C protecting layer for PtCo alloys.

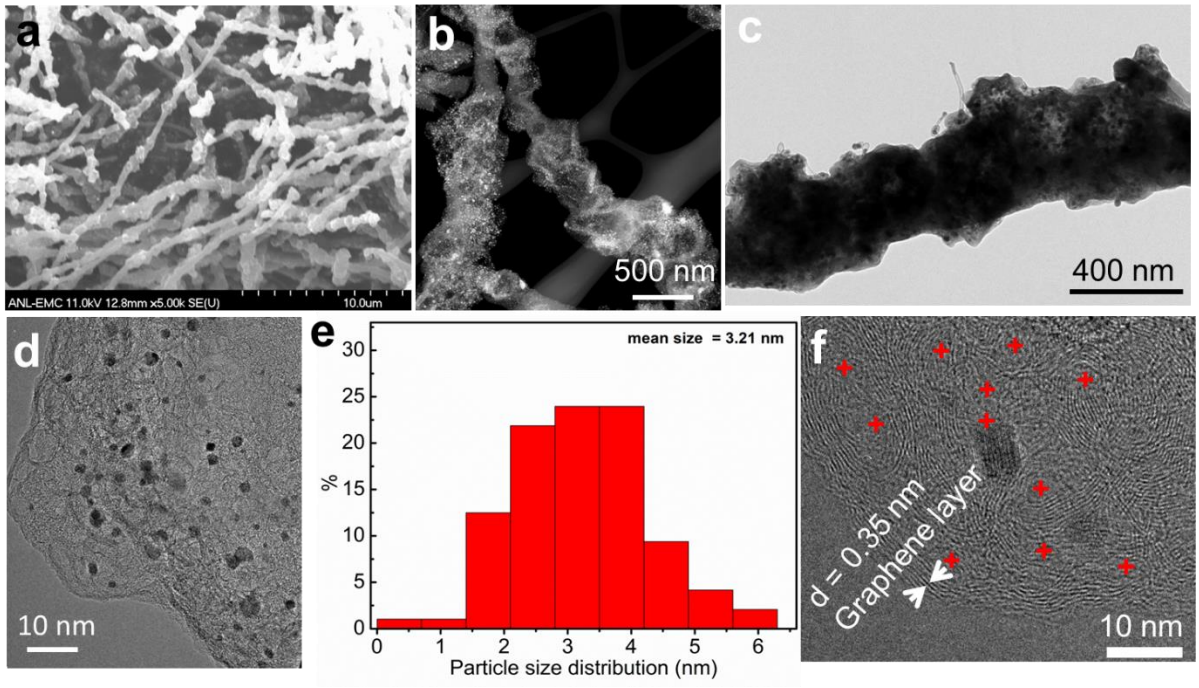

Supplementary Fig. 2 | a, SEM image of CoMOF/PAN fiber. The MOF crystals are connected by PAN fiber. The diameter of the CoMOF/PAN fiber is around ~ 500 nm. **b**, and (**c**) HAADF-STEM images of PtCo@Pt-Co-GNF, showing "beads" connected by "string". Individual fiber has an average diameter of ~ 300 nm. The beads were converted from the Co-MOF maintaining the MOF structure. **d**, HRTEM image of PtCo@Pt-Co-GNF. **e**, Particle size distribution. **f**, HRTEM image of PtCo@Pt-Co-GNF from "string" part, showing the high graphitization and the graphene layers, as well as the abundant micro-pores (red crosses).

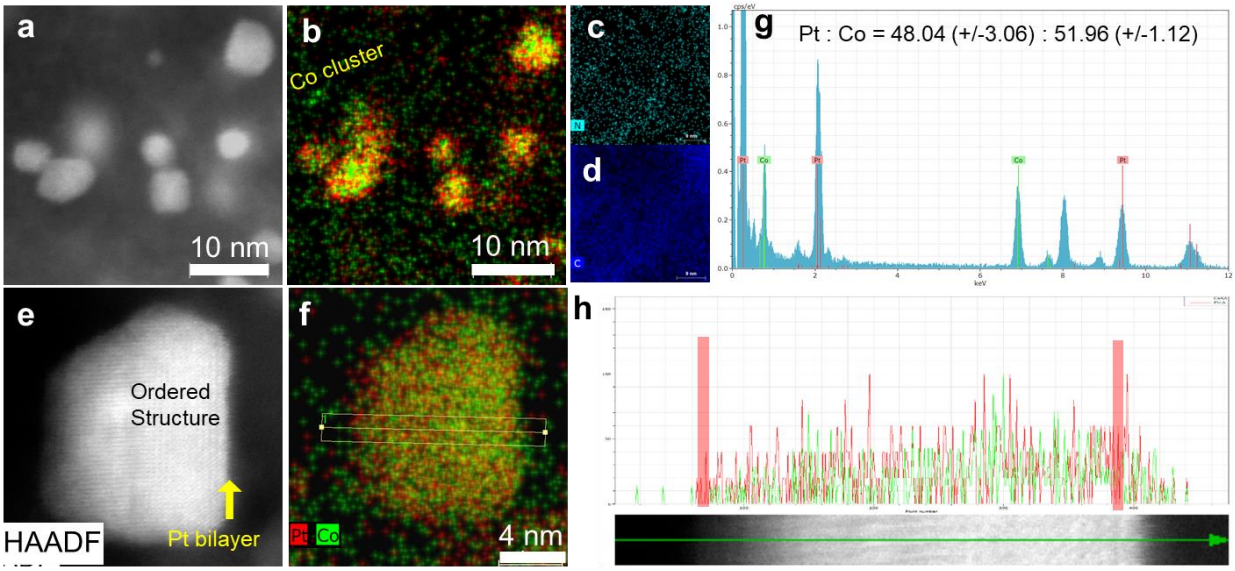

Supplementary Fig. 3 | a, HAADF-STEM image of PtCo alloy NPs in fresh PtCo@Pt-Co-GNF; **b**, the corresponding Pt vs Co elemental mapping, the corresponding carbon **c** and nitrogen **d** mapping; **g**, average atomic ratio of Pt to Co for PtCo NP. Measurement was taken over 100 NPs. **e**, Atomic resolution Z-contrast HAADF-STEM image of a representative PtCo NP; **f**, **h**, the corresponding Line-scan.

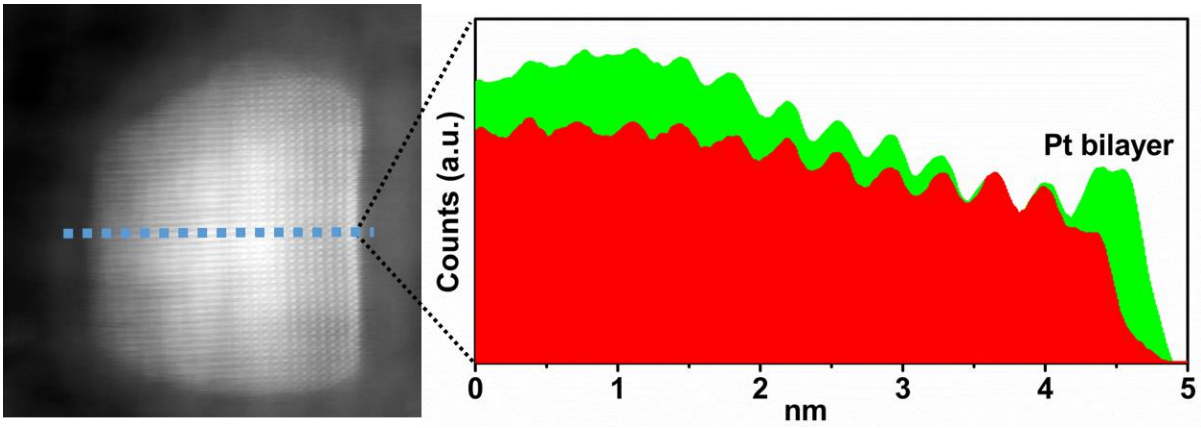

Supplementary Fig. 4| Contrast intensity profile indicates the Pt bilayer of the shell.

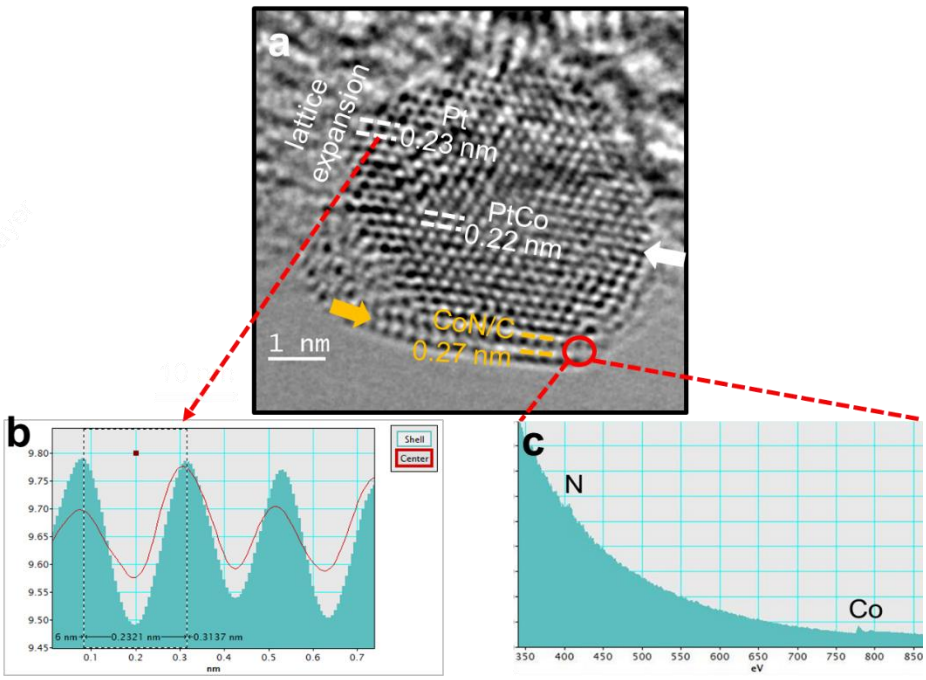

Supplementary Fig. 5 | a, HRTEM image of an individual PtCo core-shell structured NP with partially coverage of CoN/C terraces in PtCo@Pt-Co-GNF, showing lattice spacing of PtCo core (2.2 Å), Pt skin (2.3 Å) and CoN/C terrace (2.7 Å). **b**, intensity profile from shell of the PtCo NP, displaying the Pt lattice spacing. **c**, EEL spectrum acquired from the terrace in the red circle confirms that the composition consists of Co and N.

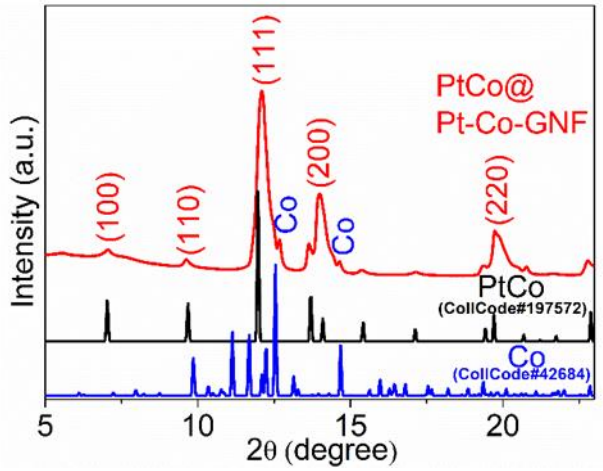

Supplementary Fig. 6 | High-energy XRD of PtCo@Pt-Co-GNF shows the Pt (100) and Pt (110) facets, conforming the formation of ordered PtCo alloy. The metallic Co is also detected, which is formed during the carbonization of Co-MOF.

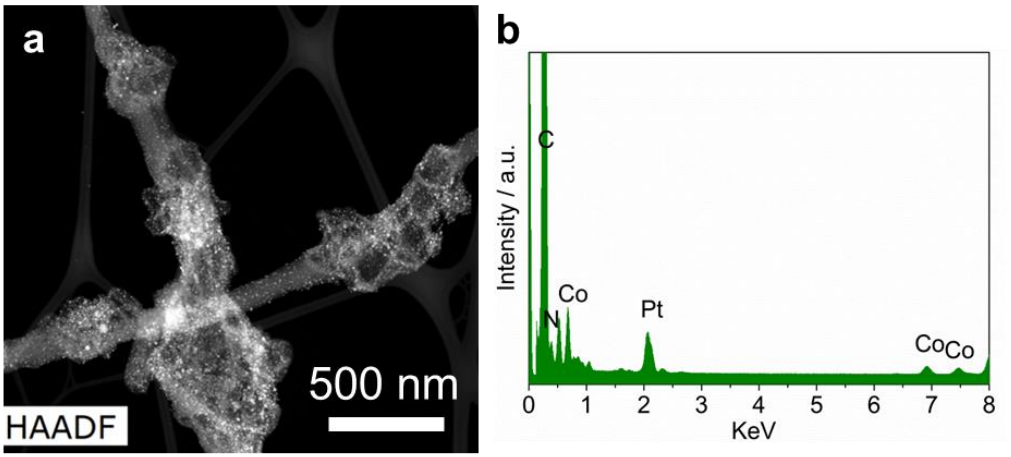

Element	at.%	Wt%
Carbon	94.0 ± 8	83.9 ± 0.9
Nitrogen	4.0 ± 0.5	4.0 ± 0.1
Cobalt	1.6 ± 0.2	6.8 ± 0.1
Platinum	0.4 ± 0.1	5.2 ± 0.1

Supplementary Fig. 7 | a, HAADF-STEM image of two single-fibers. **b**, STEM-EDS elemental analysis. The spectrum was recorded from (**a**). The Co:Pt ratio represents an average value of multiple large areas of the sample. The average atomic ratios and weight ratios of C:N:Co:Pt are listed in the table.

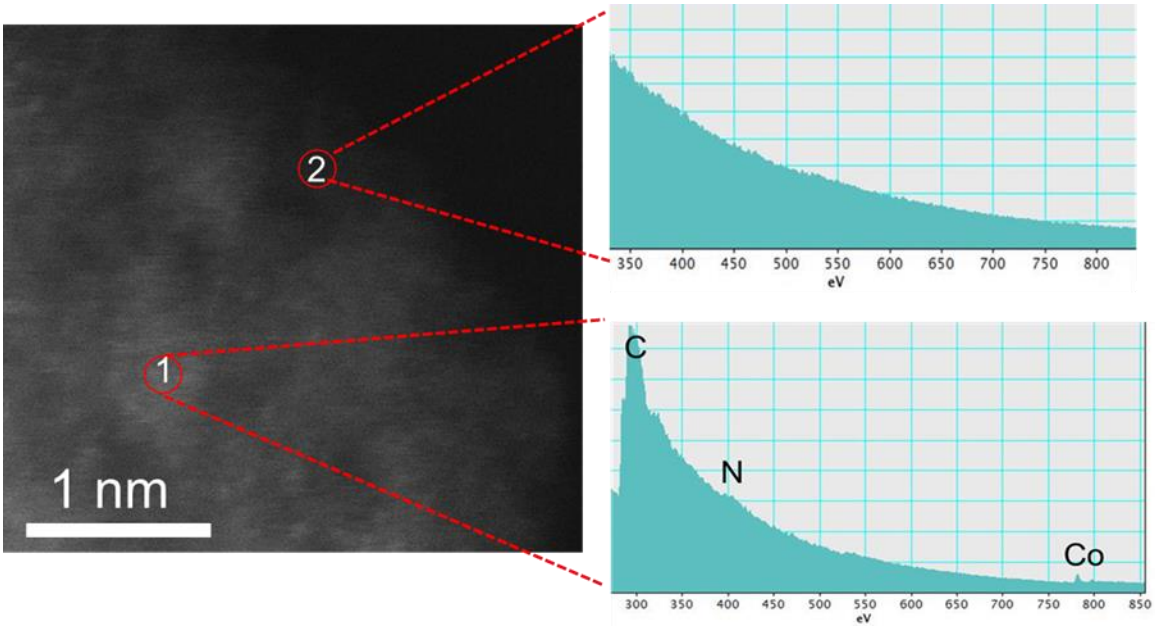

Supplementary Fig. 8 | Atomic resolution HAADF-STEM image of carbon part in PtCo@Pt-Co-GNF sample, and the EEL spectra of the N K-edge and Co L-edge acquired from the areas with (1) and without (2) bright dots, revealing that the single Co atoms were embedded in the carbon matrix presenting together with N.

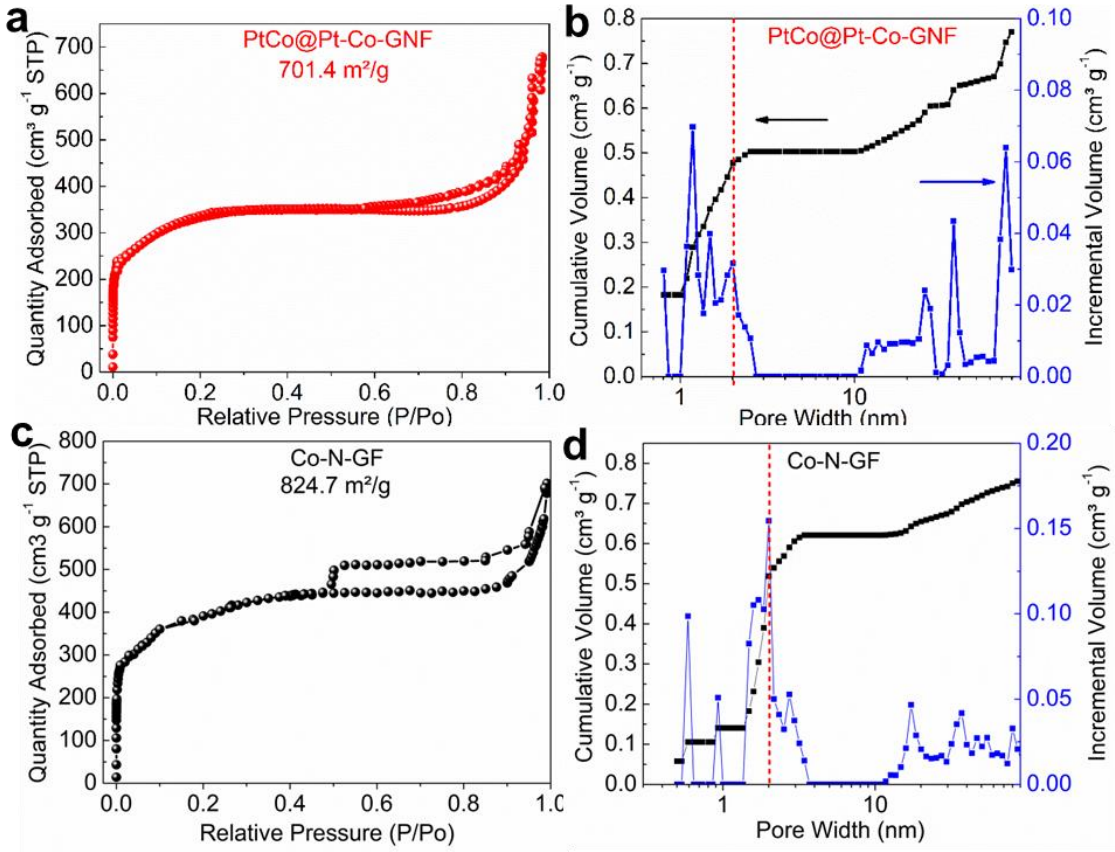

Supplementary Fig. 9 | N_2 adsorption - desorption isotherms of **a**, PtCo@Pt-Co-GNF and **c**, Co-N-GF; the corresponding pore size distribution of **b**, PtCo@Pt-Co-GNF and **d**, Co-N-GF.

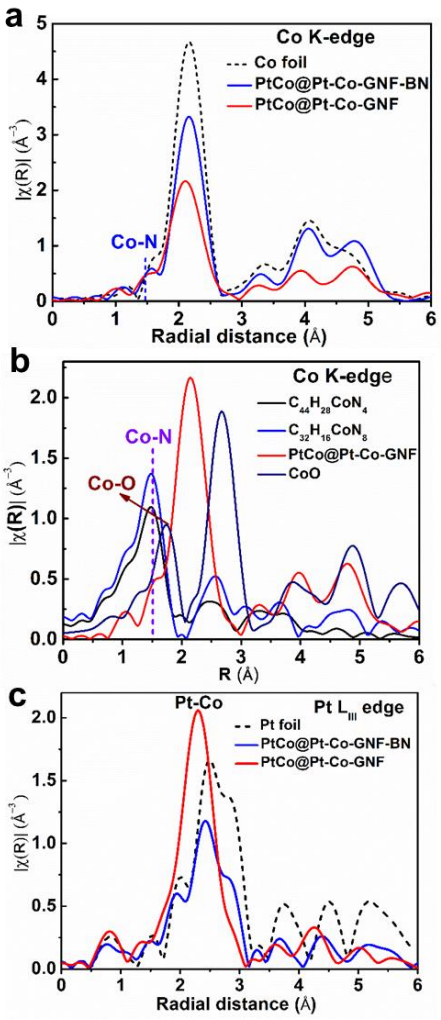

Supplementary Fig. 10 | Fourier transforms of the EXAFS spectra at Co K-edge (**a**) and Pt L_{III}-edge (**c**) for PtCo@Pt-Co-GNF before (PtCo@Pt-Co-GNF-BN) and after NH_3 treatment, as well as the references. **b**, EXAFS spectra at Co K-edge for PtCo@Pt-Co-GNF, and the references.

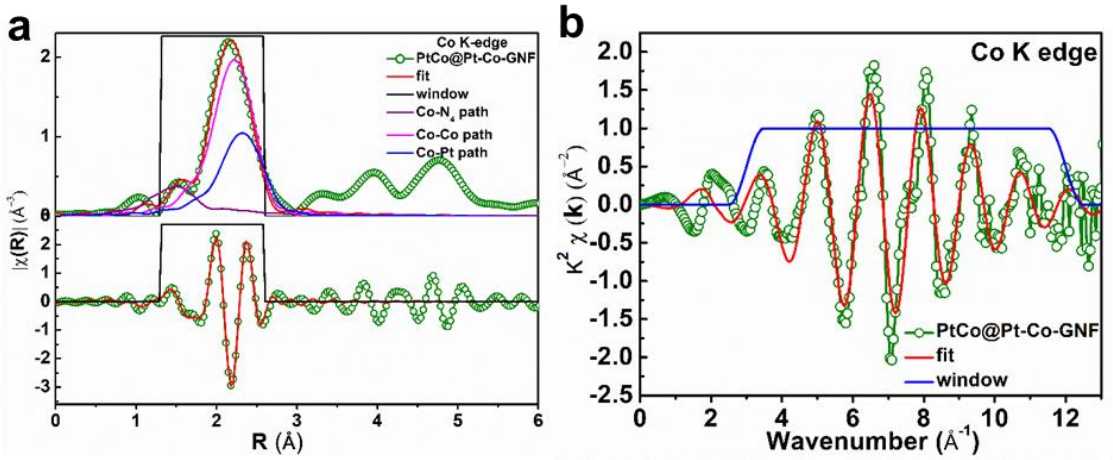

Supplementary Fig. 11 | EXAFS oscillations collected at Co K-edge of PtCo@Pt-Co-GNF (ex-situ) and the fits. **a,** EXAFS fitting curves in R-space (upper panel) and real component (Re[χ(R)]) (lower panel) at Co K-edge. **b,** k^2-weighted EXAFS oscillations collected at Co K-edge and the fits. The fitting results were shown in Supplementary Table 5.

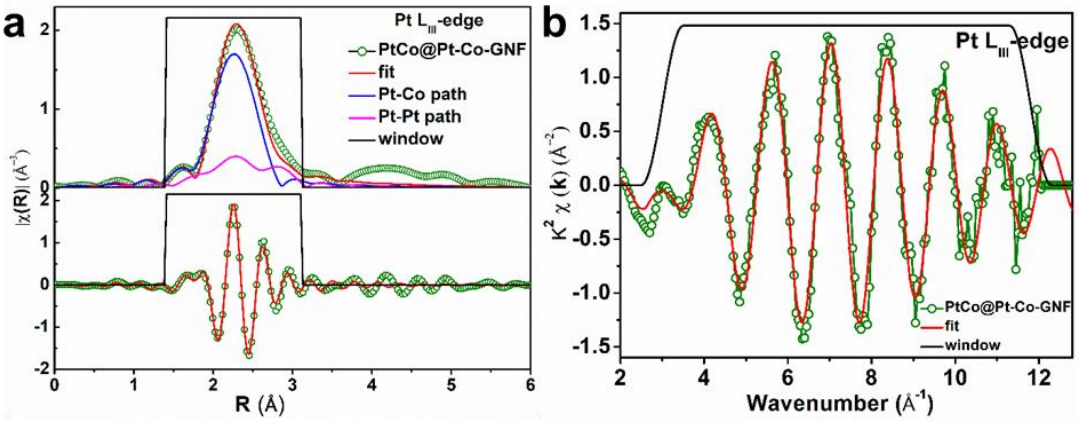

Supplementary Fig. 12 | EXAFS oscillations collected at Pt L_{III} edge of PtCo@Pt-Co-GNF (ex-situ) and the fits. **a,** EXAFS fitting curves in R-space (upper panel) and real component (Re[χ(R)]) (lower panel) at Pt L_{III}-edge. **b,** k^2-weighted EXAFS oscillations collected at Pt L_{III}-edge and the fits. The fitting results were shown in Supplementary Table 5.

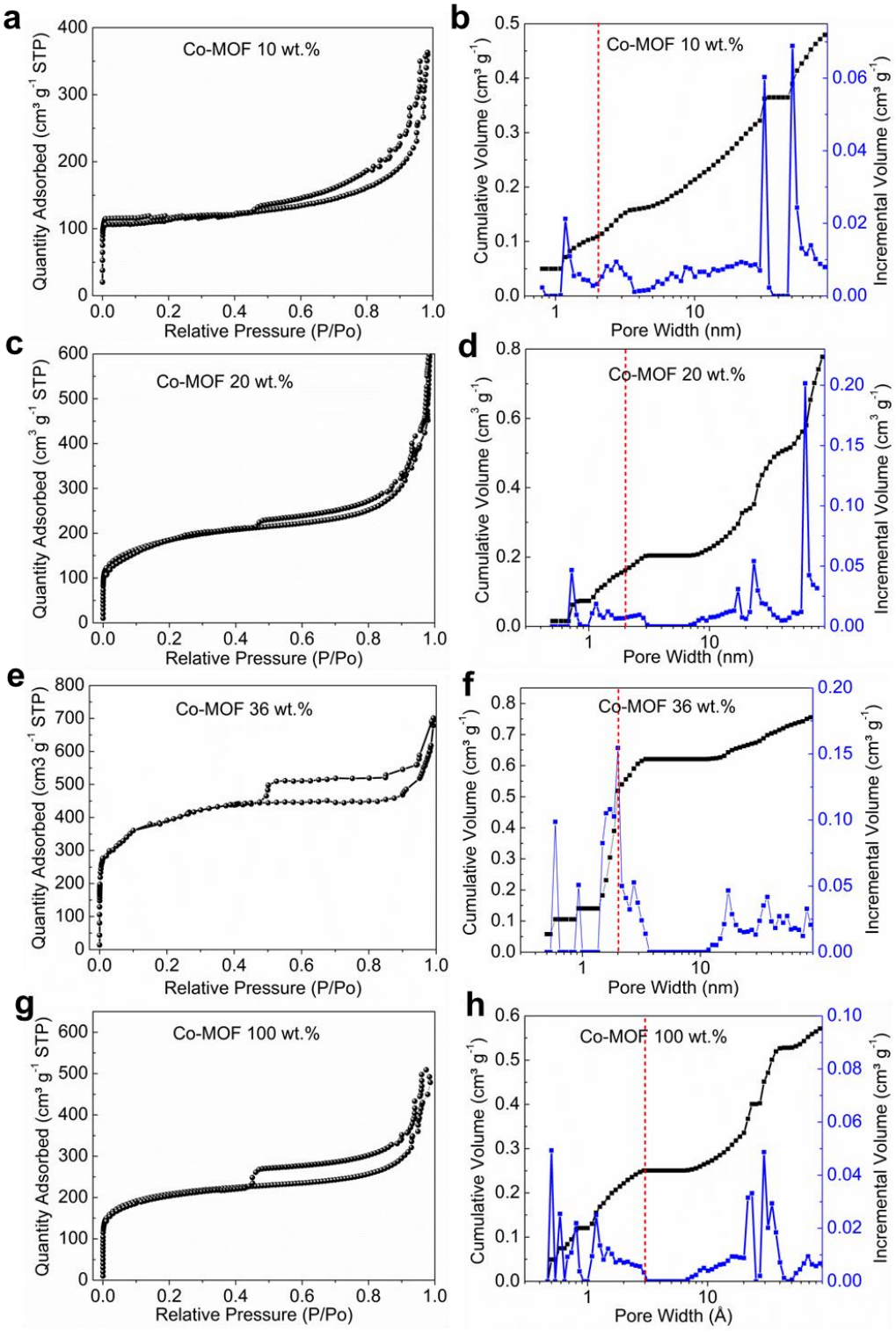

Supplementary Fig. 13 | BET surface area (**a, c, e, g**) and pore size distribution (**b, d, f, h**) for Co-N-GF samples with different CoMOF contents in the CoMOF/PAN fiber precursors.

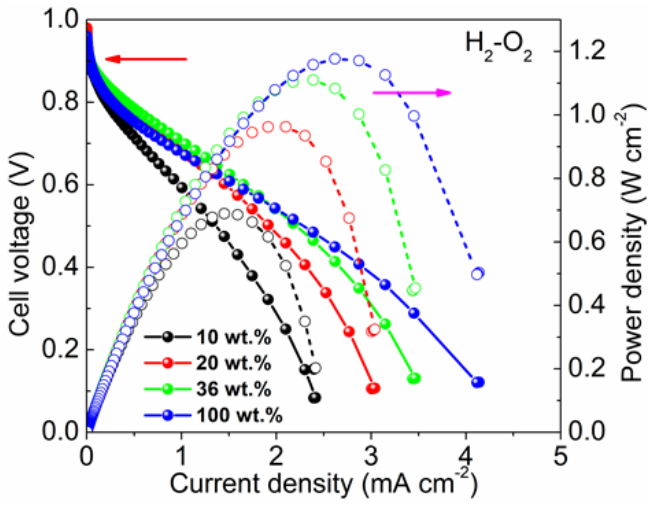

Supplementary Fig. 14 | H_2-O_2 fuel cell performance of fibrous catalysts prepared with various CoMOF concentration in the CoMOF/PAN fiber precursors (denoted as "x wt.%"), where "x" indicates the concentration of Co-MOF. Fuel cell performance of PtCo@Pt-Co-GNF shows a higher current in the kinetic region relative to that of catalyst prepared from CoMOF (100 wt.%), ascribing to the higher BET surface area and micro-pore concentration of the former. The inferior performances of catalysts prepared with CoMOF (10 wt.%), CoMOF (20 wt.%) relative to that of PtCo@Pt-Co-GNF, originate from their lower Co-N_x active sites concentration. Test condition: 80 ^{o}C, 100% RH, 150 KPa_{abs}, membrane = Nafion®211, anode loading ≤ 0.035 mg_{Pt} cm^{-2}, cathode Pt loading ≤ 0.048 mg_{Pt} cm^{-2}, H_2 flow rate = O_2 flow rate = 200 mL min^{-1}.

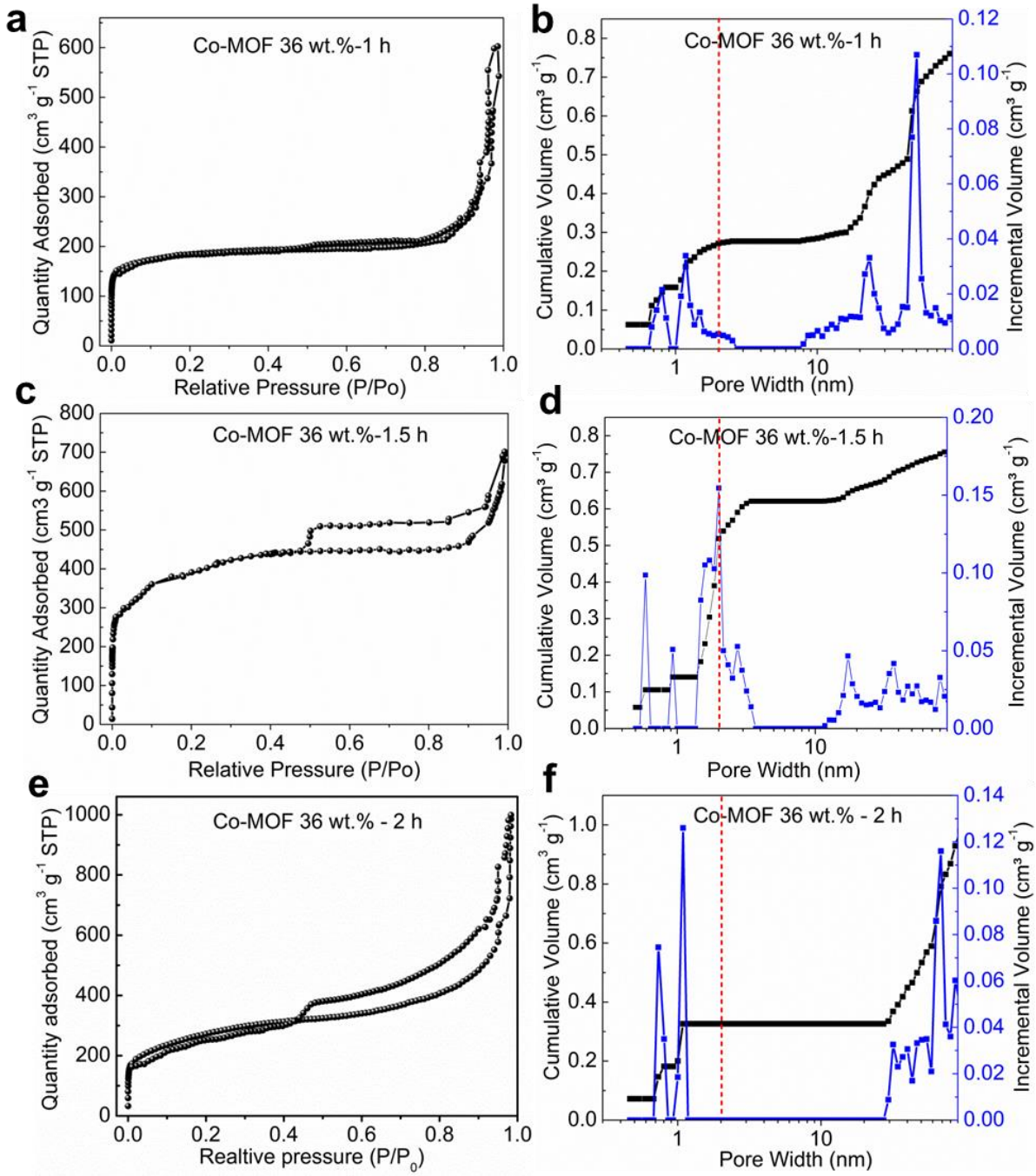

Supplementary Fig. 15 | BET surface area (**a, c, e**) and pore size distribution (**b, d, f**) of Co-N-GF (Co-MOF, 36 wt.%) pyrolyzed at 1000 ^{o}C for different times.

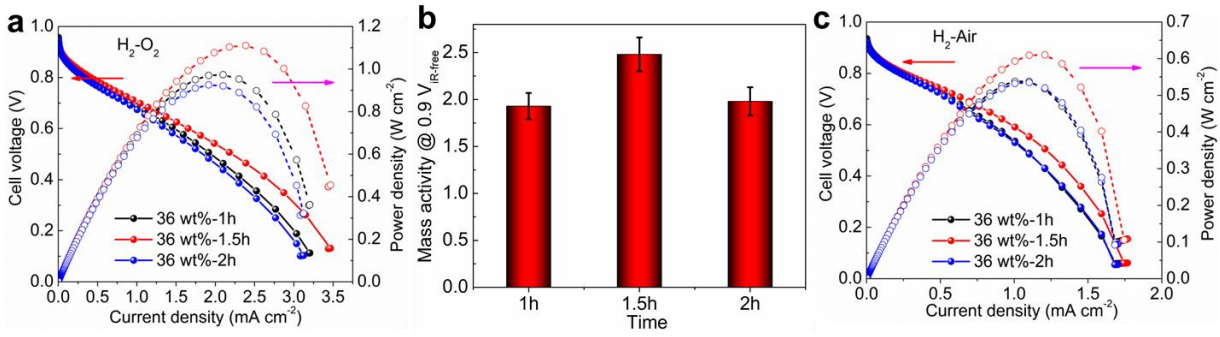

Supplementary Fig. 16 | a, H_2-O_2 fuel cell performances of catalysts prepared with Co-N-GF(Co-MOF, 36 wt%) obtained at 1000 °C for different pyrolysis times. **b**, the corresponding MA at 0.9 $V_{iR\text{-}free}$ voltage. **c**, the corresponding H_2-Air fuel cell performances. Test condition: 80 °C, 100% relative humidity RH, 150 KPa_{abs}, membrane = Nafion® 211, anode loading = 0.035 mg_{Pt} cm^{-2}, cathode Pt loading = ~ 0.048 mg_{Pt} cm^{-2}, H_2 flow rate = O_2 flow rate = 200 mL min^{-1} in H_2-O_2 cell, and H_2 flow rate = 200 mL min^{-1} & Air flow rate = 780 mL min^{-1} in H_2-Air cell.

The micropore is essential for PGM-free catalyst to achieve high activity[1,2]. It should be emphasized that Co-MOF plays a critical role in tuning the pore structure and Co-N_x population of the final catalyst to achieve the highest ORR activity. To elucidate this point, we investigated the Co-MOF concentration in the Co-MOF/PAN fiber precursor along with different pyrolysis time (Supplementary Fig. 13 and Fig. 15). With increasing concentrations of Co-MOF from 10% to 36%, the BET surface area of the obtained Co-N-GF increased from 393.3 to 824.7 m^2 g^{-1}, the volume of the micropore increased from 0.11 cm^3 g^{-1} to 0.53 cm^3 g^{-1} (Supplementary Table 2). A higher concentration of Co-MOF leads to better fuel cell performance (Supplementary Fig. 14). Next, we discussed the Co-MOF/PAN fiber with 36% Co-MOF concentration pyrolyzed at 1000 °C in Ar for 1 h, 1.5 h and 2 h. With prolonged pyrolysis time, even though the BET surface area increased to 1200 m^2 g^{-1}, the micropore volume decreased after pyrolysis for 1.5 h (Supplementary Fig. 15, Supplementary Table 3), resulting in a lower fuel cell activity (Supplementary Fig. 16). The Pt mass activity of the corresponding PEMFCs ranged from 1.93 ± 0.14 to 2.48 ± 0.18 A mg_{Pt}^{-1} (Supplementary Fig. 16**b**). The highest fuel cell activity was achieved with Co-N-GF(36 wt%)

pyrolyzed for 1.5 h. Hence, after the optimization with CoMOF concentration of 36% in the CoMOF/PAN fiber precursor, and pyrolyzed for 1.5 h in flowing Ar, the obtained Co-N-GF exhibits a high BET surface area with appropriate porosity possessing the balanced micro-/meso-/macro-pore structure in a well-defined network architecture.

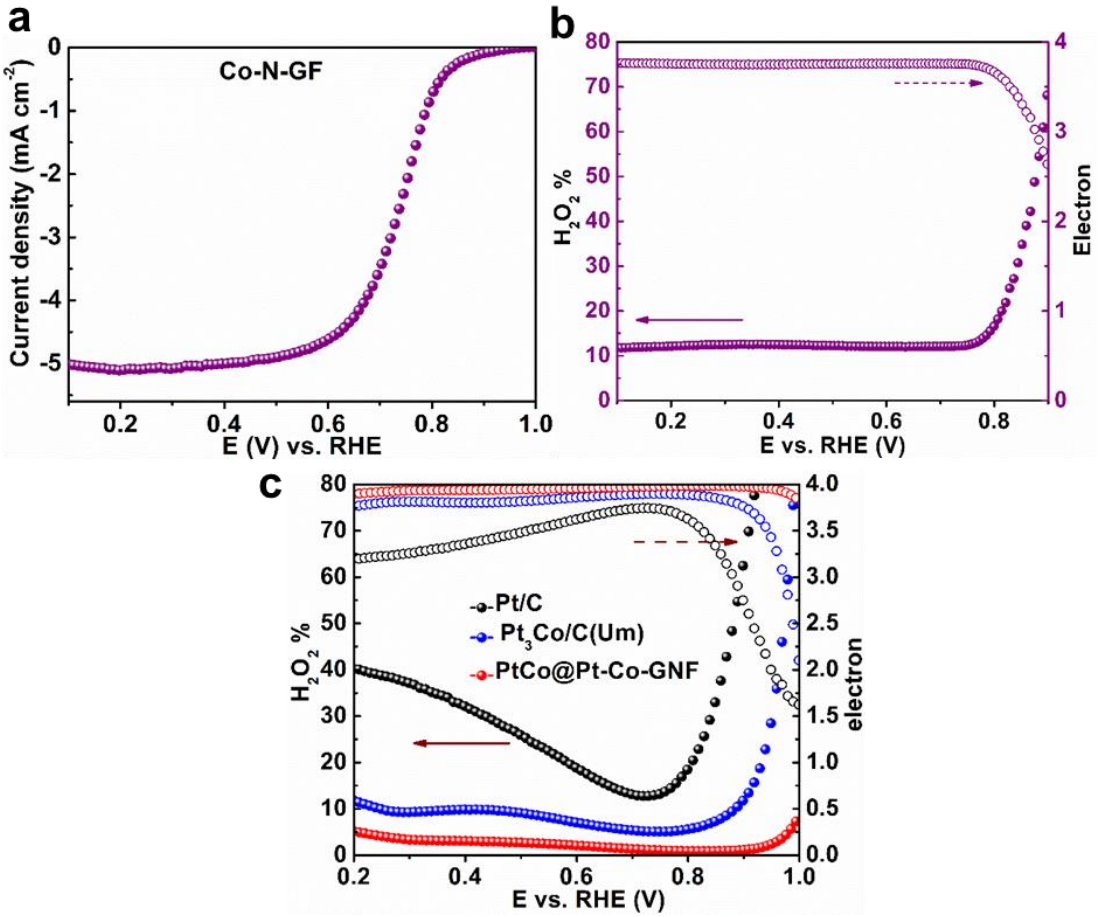

Supplementary Fig. 17 | **a**, The LSV of Co-N-GF substrate, showing half-wave potential of 0.75 V and onset potential of 0.93 V. **b**, the corresponding H_2O_2 yield and electron transfer number. **c**, The H_2O_2 yield and electron transfer number of PtCo@Pt-Co-GNF, Pt/C and Pt_3Co/C(Um) obtained from Fig. 3a in the main text. The H_2O_2 yield was reduced from ~ 11% for Co-N-GF to less than 5 % for PtCo@Pt-Co-GNF. The electron transfer was improved from 3.77 for Co-N-GF to 3.99 for PtCo@Pt-Co-GNF.

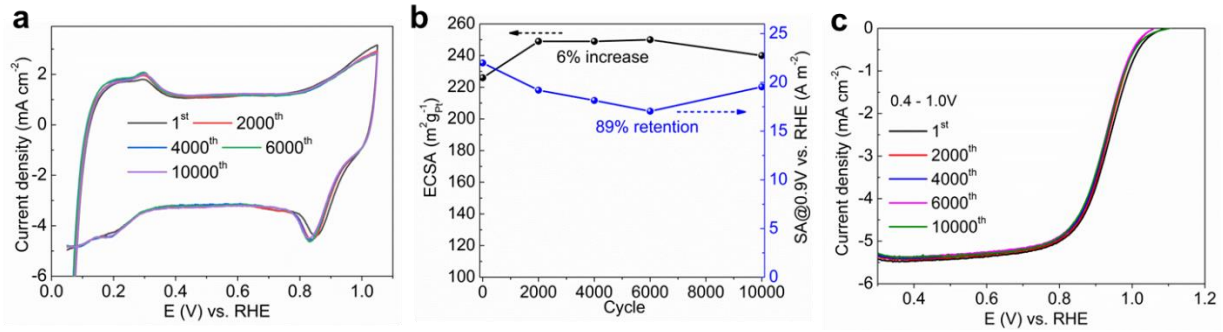

Supplementary Fig. 18 | a, CV curves of PtCo@Pt-Co-GNF at selective cycles. **b**, the evolution of ECSA and SA@0.9 V of PtCo@Pt-Co-GNF as function of the cycle numbers. **c**, LSV curves of PtCo@Pt-Co-GNF at selective cycles. The durability measurements were conducted by sweeping the potential between 0.4 V and 1.0 V by RRDE method in O_2 saturated 0.1 M $HClO_4$ electrolyte. Pt loading was ~ 4 μg cm^{-2}.

Electrochemical active surface area (ECSA) is believed to be an important contributor to catalyst activity. We calculate the ECSA of PtCo@Pt-Co-GNF by measuring the charge collected in the H_{upd} absorption /desorption region after double-layer correction and assuming a value of 210 μc cm^{-2} for the absorption of a hydrogen monolayer[3]. At room temperature, the PtCo@Pt-Co-GNF exhibited ECSA of 226 m^2 g_{Pt}^{-1} (Supplementary Fig. 18**b**). The high ECSA may result from the unique hierarchical porous structure of the interconnected nanofiber support that increases the accessibility of Pt to the reactant and ionomer, also shortens the ionic diffusion length in the electrode. The catalyst is very stable. We observed a slightly increase in ECSA (240 m^2 g_{Pt}^{-1}), and only 6 mV voltage loss in half-wave potential ($E_{1/2}$) after 10 000 cycles.

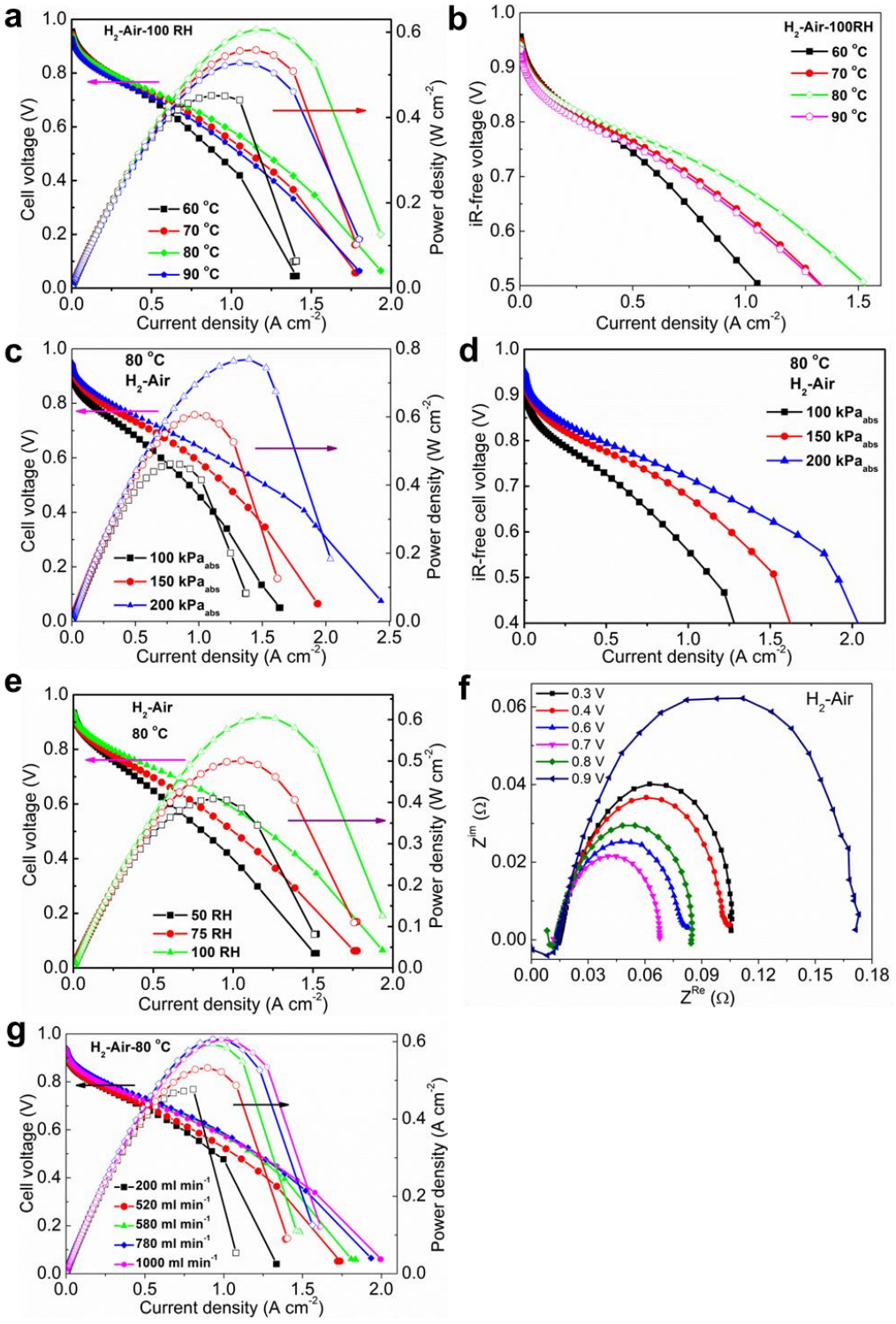

Supplementary Fig. 19 | H_2-Air fuel cell performance investigations for MEA with PtCo@Pt-Co-GNF as cathodic catalyst under different test condition: **a**, 150 KPa_{abs}, 100%RH, different temperatures of 60 °C, 70 °C, 80 °C, 90 °C; **b**, iR corrected polarization curves obtained from (**a**); **c**, 80 °C, 100%RH, different pressure of 100 KPa_{abs}, 150 KPa_{abs}, 200 KPa_{abs}; **d**, iR corrected polarization curves obtained from (**c**), showing the large current produced by PtCo@Pt-

Co-GNF. **e**, 80 ^{o}C, 150 KPa_{abs}, different RH of 50%, 75%, 100%; **f**, 80 ^{o}C, 100%RH, 150 KPa_{abs}, 1-10000 Hz, EIS at different voltage of 0.3 V, 0.4 V, 0.6 V 0.7 V, 0.8 V, 0.9 V; **g**, 80 ^{o}C, 150 KPa_{abs}, 100%RH, different Air flow rate of 200, 520, 580, 780 and 1000 ml min^{-1}. All the tests were conducted on the same MEA: membrane = Nafion®211, anode loading ≤ 0.035 mg_{Pt} cm^{-2}, cathode Pt loading ≤ 0.048 mg_{Pt} cm^{-2}, H_2 flow rate = 200 mL min^{-1}, air flow rate = 780 ml min^{-1} for (**a**) to (**f**).

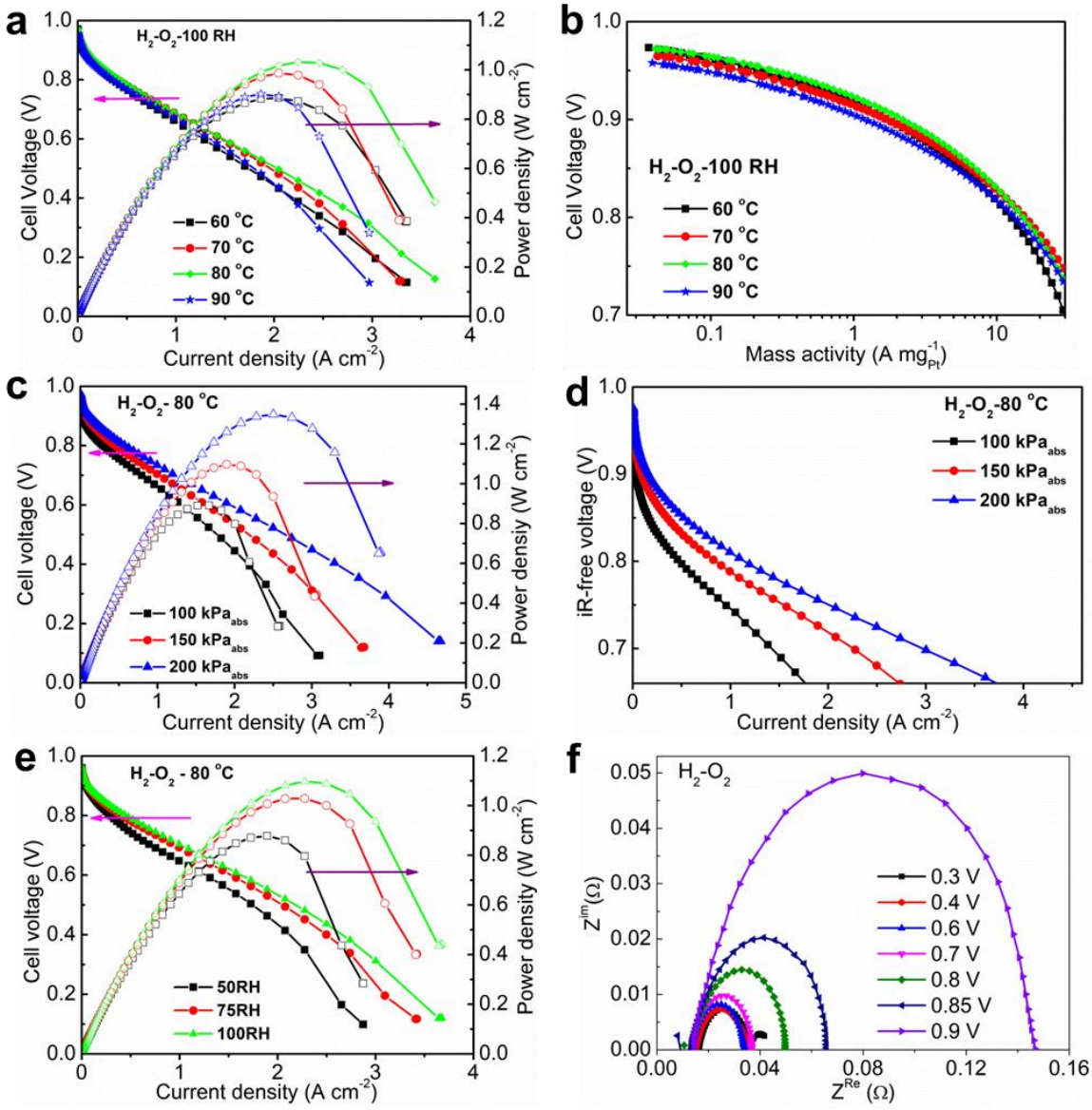

Supplementary Fig. 20 | H_2-O_2 fuel cell performance investigations for MEA with PtCo@Pt-Co-GNF as cathodic catalyst under different test condition, **a**, 150 KPa_{abs}, 100%RH, different temperatures of 60 °C, 70 °C, 80 °C, 90 °C; **b**, the corresponding Tafel plot of mass activity; **c**, 80 °C, 100%RH, different pressure of 100 KPa_{abs}, 150 KPa_{abs}, 200 KPa_{abs}; **d**, iR corrected polarization curves obtained from (**c**), showing the large current produced by PtCo@Pt-Co-GNF; **e**, 80 °C, 150 KPa_{abs}, different RH of 50%, 75%, 100%; **f**, 80 °C, 100%RH, 150 KPa_{abs}, 1-10000 Hz, EIS at different voltage of 0.3 V, 0.4 V, 0.6 V 0.7 V, 0.8 V, 0.85 V, 0.9 V. The slightly high Rct + Rmt at 0.9 V is due to the membrane less hydrated at 0.9 V. All the tests were conducted on the same MEA: membrane = Nafion® 211, anode loading ≤ 0.035 mg_{Pt} cm^{-2}, cathode Pt loading ≤ 0.048 mg_{Pt} cm^{-2}, H_2 flow rate = O_2 flow rate = 200 mL min^{-1}.

We also studied the effects of various parameters including temperature, pressure, RH, and resistance that related to water management on fuel cell performance (Supplementary Fig. 19 and Fig. 20). The activities of both H_2-O_2 cell and H_2-Air cell were enhanced with increasing temperature from 60 ^oC to 80 ^oC, which is attributed to the increased gas diffusivity and membrane conductivity at higher temperature. Increasing temperature to 90 ^oC resulted in dry-out of the membrane and poor conductivity, manifesting itself as a performance decrease. Even at 60 ^oC, the Pt MA of PtCo@Pt-Co-GNF is still as high as 1.80 ± 0.13 A g_{Pt}^{-1}. The Pt MA of 2.48 ± 0.18 A g_{Pt}^{-1} at 80 ^oC and 150 KPa_{abs}, is the highest achieved ever in an operating fuel cell (Supplementary Table 4). Fuel cell performances at different absolute pressure: 100 KPa_{abs}, 150 KPa_{abs}, 200 KPa_{abs} were shown in Supplementary Fig. 19**c, d**, and Fig. 20**c, d**. As operating pressure increased, the fuel cell performance improved. The H_2-O_2 cell and H_2-Air cell reached maximum power densities of 1.36 W cm^{-2} and 0.77 W cm^{-2} at 200 KPa_{abs}, corresponding to an effective Pt utilization of 0.041±0.003 g_{Pt} kW^{-1} on the cathode in H_2-O_2 cell, and 13.8 kW g_{Pt}^{-1} in H_2-Air cell, suggesting a high efficiency of PtCo@Pt-Co-GNF toward ORR in PEMFC. The results rank the highest reported so far (Fig. 3**h**).

Electrochemical impedance spectroscopy (EIS) has a significant impact on the electron transfer property of the support, and the higher catalytic performance is believed to be associated with an improved electrical conductivity. EIS data is represented as Nyquist plot extracted to be ohmic resistance (Rohm), charge transfer resistance (Rct) and mass transport resistance (Rmt). H_2-Air (Supplementary Fig. 19**f**) and H_2-O_2 cell (Supplementary Fig. 20**f**) cell show very low Rct and Rmt, displaying the high conductivity and excellent water management property of Co-N-GF support due to the formation of P-type graphene and the hierarchical interconnected pore structure. We observed a decrease in limiting current density at low RH due to reduction in concentration of the reactant gas. Performance loss caused by the mass transport is barely noticeable at 100% RH (Supplementary Fig. 19**e** and Fig. 20**e**). H_2-Air fuel cell performance is improved as increasing the air gas flow rate from 200 ml min^{-1} to 520 ml min^{-1} due to the increased O_2 concentration to the cathode layer, which increases the reaction rate. The increase in H_2-Air cell performance is not obvious from 580 ml min^{-1} to 1000 ml min^{-1}, implying that the rationally designed porous structure compensates the mass transport limitation. We attribute the unprecedented fuel cell performance to the high surface area, the unique hierarchical porous interconnected-pore structure, the

synergistic effect between PGM and PGM-free active sites, the excellent electron conductivity and the corrosion resistance of the support.

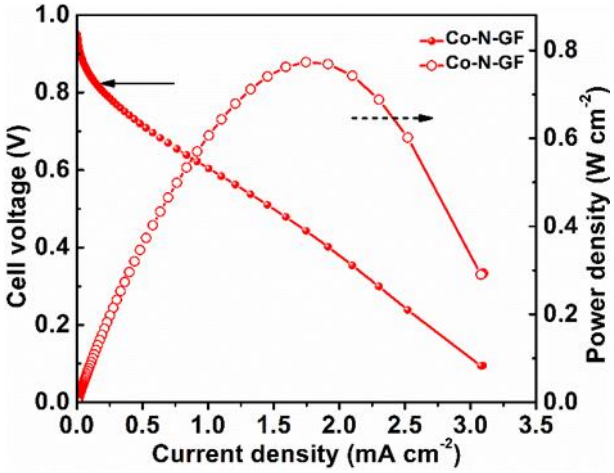

Supplementary Fig. 21 | H_2-O_2 fuel cell performances of Co-N-GF. Test condition: 80 ºC, 100% relative humidity RH, 150 KPa_{abs}, membrane = Nafion® 211, anode Pt loading = 0.2 mg_{Pt} cm^{-2}, cathode PGM-free catalyst loading = ~ 3.6 mg cm^{-2}, H_2 flow rate = O_2 flow rate = 200 mL min^{-1}.

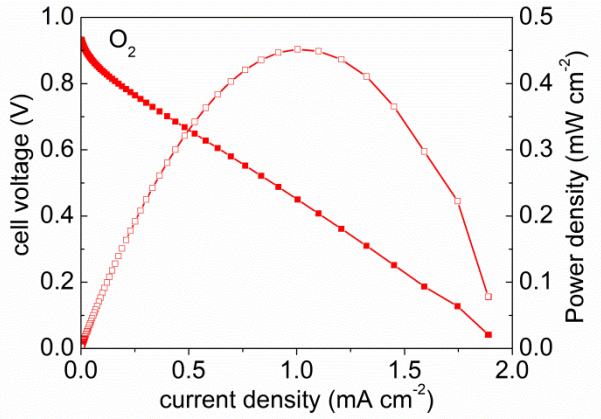

Supplementary Fig. 22 | H_2-O_2 fuel cell performance of PtCo/XC-72 synthesized by using the same method as that used in PtCo@Pt-Co-GNF catalyst for Pt synthesis. PtCo concentration in PtCo/XC-72 catalyst is ~ 5 wt%. Test condition: 80 ºC, 100% relative humidity RH, 150 KPa_{abs}, membrane = Nafion® 211, anode loading = 0.035 mg_{Pt} cm^{-2}, cathode Pt loading = ~ 0.06 mgPt cm^{-2}, H_2 flow rate = O_2 flow rate = 200 mL min^{-1}.

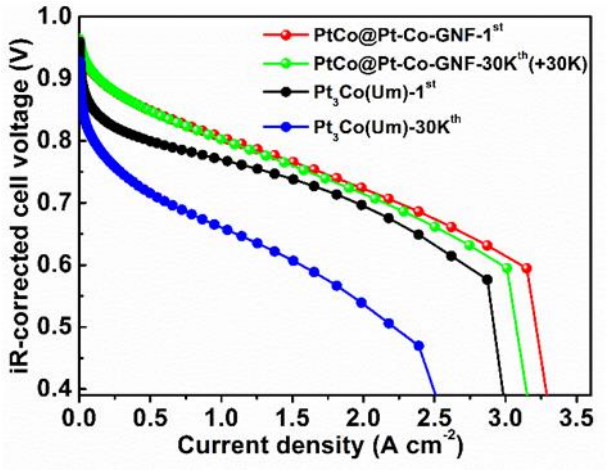

Supplementary Fig. 23 | IR-corrected polarization curves of H_2-O_2 cell obtained from Fig. 3**f** in the main text, showing that PtCo@Pt-Co-GNF possessing significant higher activity than that of Pt_3Co (Um) in the kinetic region > 0.78 V. No discernable degradation was observed for PtCo@Pt-Co-GNF catalyst after 60,000 AST cycles including 30,000 AST cycles in H_2-Air cell and a continued 30,000 AST cycles in H_2-O_2 cell. However, the Pt_3Co (Um) was seriously degraded.

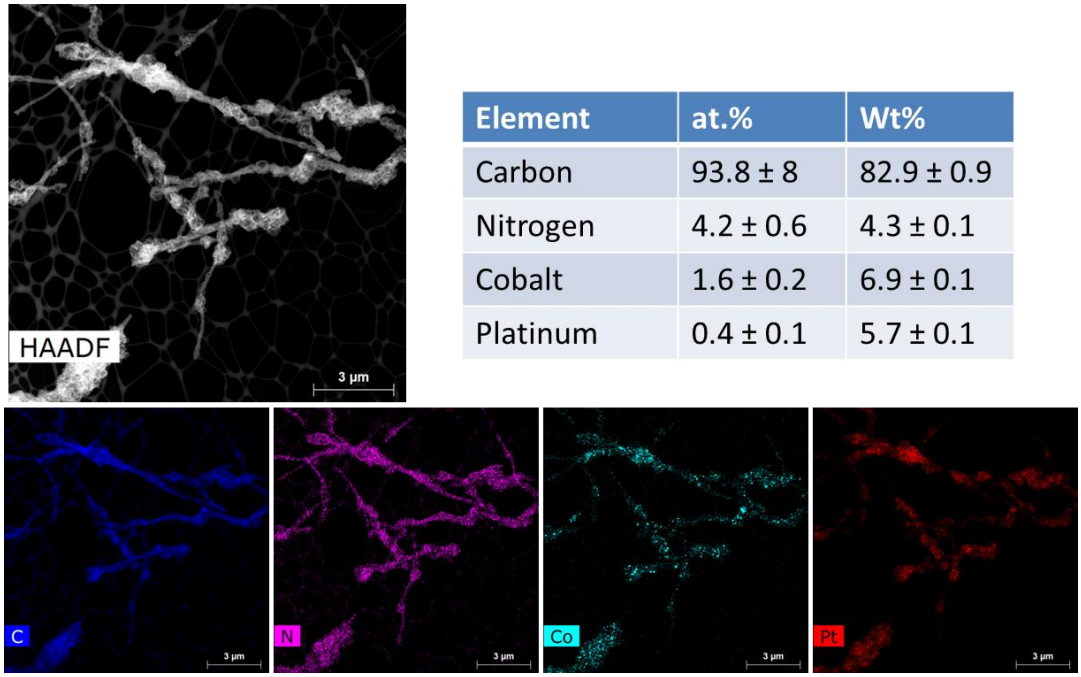

Element	at.%	Wt%
Carbon	93.8 ± 8	82.9 ± 0.9
Nitrogen	4.2 ± 0.6	4.3 ± 0.1
Cobalt	1.6 ± 0.2	6.9 ± 0.1
Platinum	0.4 ± 0.1	5.7 ± 0.1

Supplementary Fig. 24 | HAADF-STEM image and the corresponding EDS elemental mapping of PtCo@Pt-Co-GNF after AST (60000 in total') in fuel cell. Sample was extracted from the cathode of the MEA after 30,000 AST test in H_2-Air cell and continued 30,000 AST test in H_2-O_2 cell. EDS elemental analysis averaged over multiple areas demonstrated that the atomic ratio and the weight ratio of C: N:Co:Pt after two consecutive ASTs in fuel cell were basically the same as the fresh sample, corroborating the durable structure of PtCo@Pt-Co-GNF under harsh PEM conditions.

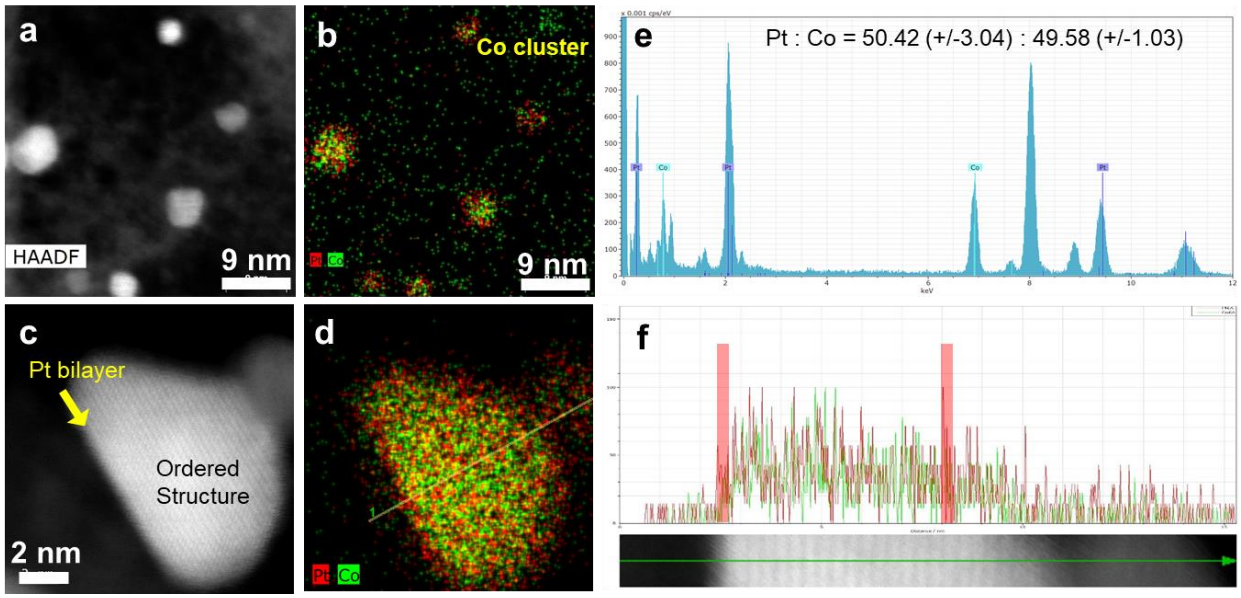

Supplementary Fig. 25 | a, HAADF-STEM image focusing on PtCo alloy in the PtCo@Pt-Co-GNF sample extracted from MEA after 60,000 AST cycles including the 30,000 AST test in H_2-Air cell and the continued 30,000 AST test in H_2-O_2 cell; **b**, corresponding EDS elemental mapping. Co cluster was also observed which was generated during carbonization of Co-MOF. It was wrapped by graphene which was hard to be leached out even by acid wash. The images revealed that the particle size of the alloy was preserved without agglomeration after the harsh AST test, further confirming the durable structure of the PtCo alloy. **c**, Atomic resolution Z-contrast-HAADF-STEM image of a representative PtCo alloy NP after AST; **d**, **f**, the corresponding Line-scan. **e**, average atomic ratio of Pt to Co of PtCo NP after AST. Measurement was taken over 100 NPs.

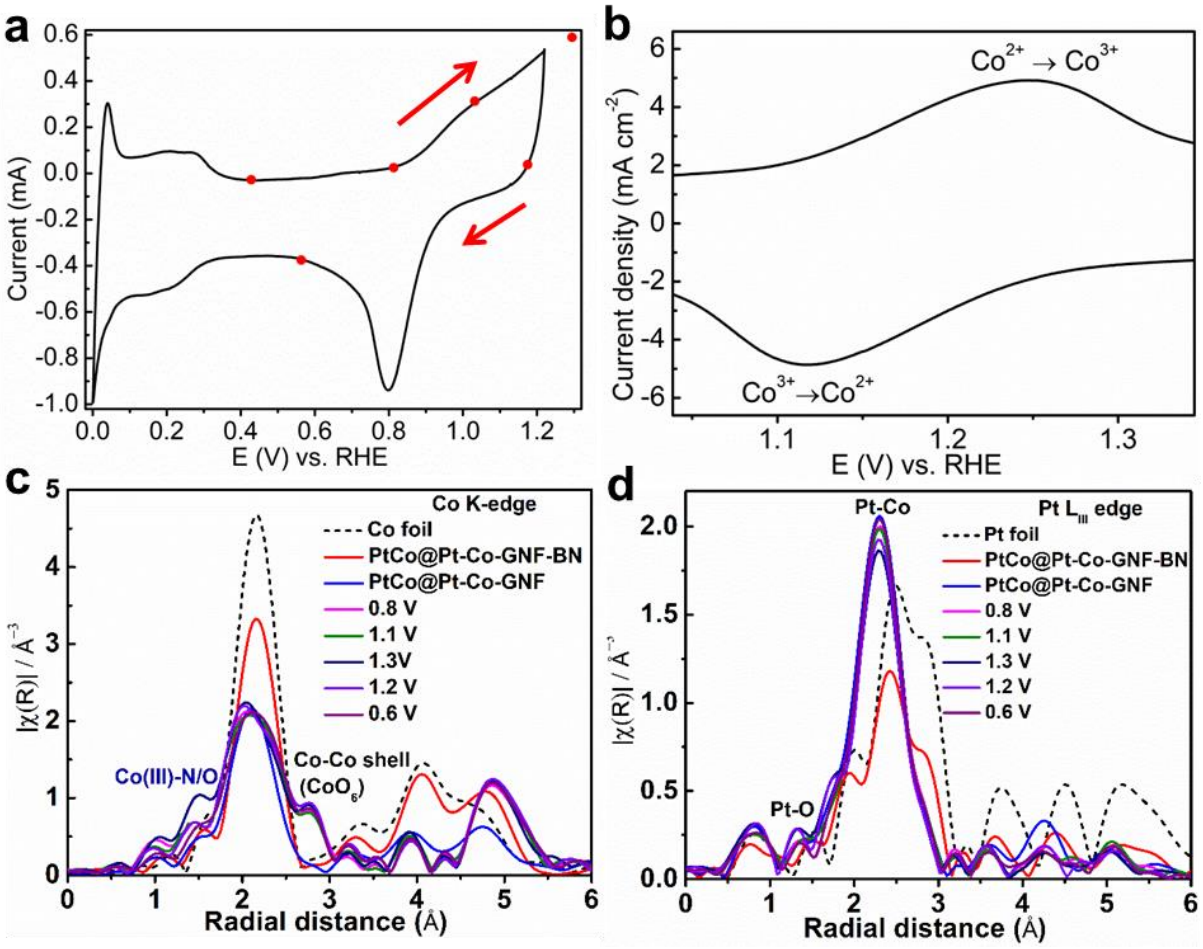

Supplementary Fig. 26 | a, Cyclic voltammetry (CV) curve depicting the potentials used for Operando XAS measurements. **b**, CV curve showing the position of redox peaks. Measured in Ar saturated 0.1 M $HClO_4$. **c**, FT EXAFS spectra at Co K-edge collected at potentials ascending from 0.8 V, 1.1 V to 1.3 V and then descending to 1.2 V and 0.6 V in O_2 saturated 0.1 M $HClO_4$ electrolyte, as well as ex-situ samples. **d**, FT EXAFS spectra at Pt L_{III}-edge collected at potentials ascending from 0.8 V, 1.1 V to 1.3 V and then descending to 1.2 V and 0.6 V in O_2 saturated 0.1 M $HClO_4$ electrolyte, as well as ex-situ samples. Co foil and Pt foil were measured as references.

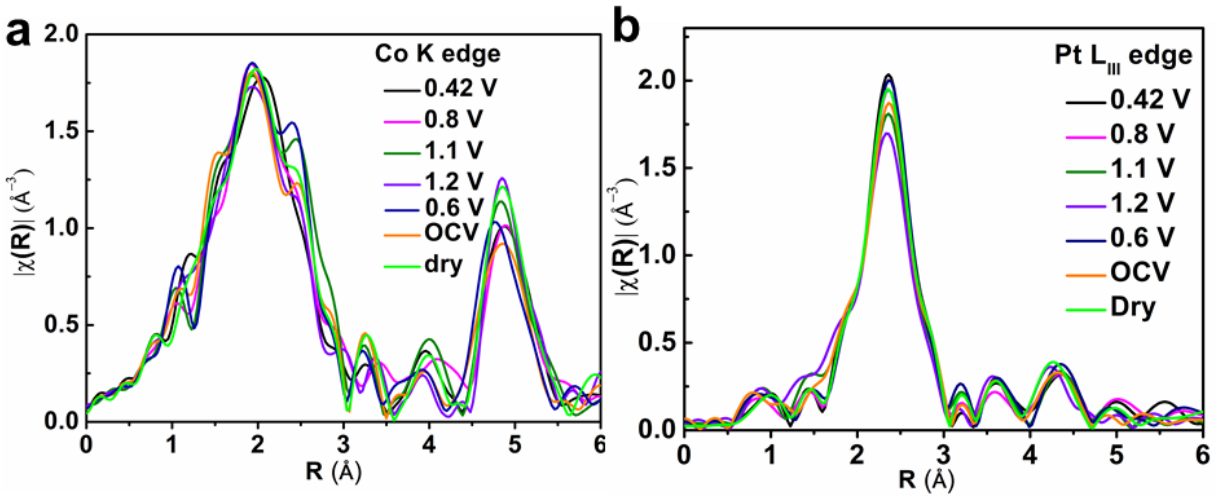

Supplementary Fig. 27 | a, FT EXAFS spectra at Co K-edge collected at potentials (OCV = ~ 0.93 V was included) ascending from 0.42 V, 0.8 V, 1.1 V, and the potential was held at 1.3 V for 15 min (no data was recorded), then descending to 1.2 V and 0.6 V in Ar saturated 0.1 M $HClO_4$ electrolyte, as well as ex-situ samples (Dry). **b**, FT EXAFS spectra at Pt L_{III}-edge collected at potentials (OCV = ~ 0.96 V was included) ascending from 0.42 V, 0.8 V, 1.1 V, and the potential was held at 1.3 V for 15 min (no data was recorded), then descending to 1.2 V and 0.6 V in Ar saturated 0.1 M $HClO_4$ electrolyte, as well as ex-situ samples (Dry).

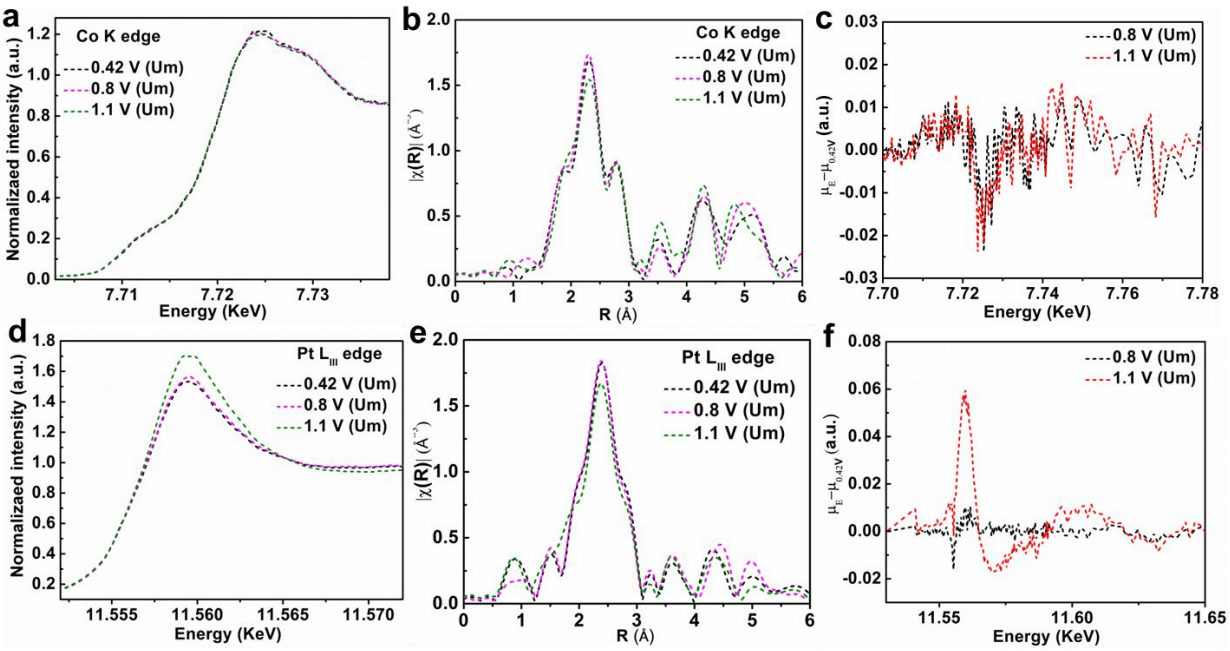

Supplementary Fig. 28 | Operando XAS measurements on $Pt_3Co/C(Um)$ in Ar saturated 0.1 M $HClO_4$ electrolyte. **a**, Co K-edge XANES spectra measured at representative potentials ascending from 0.42 V, 0.8 V to 1.1 V. **b**, Co K-edge EXAFS spectra recorded at representative potentials ascending from 0.42 V, 0.8 V to 1.1 V. **c**, differential Δμ XANES spectra at Co K edge. **d**, Pt L_{III}-edge XANES spectra measured at representative potentials ascending from 0.42 V, 0.8 V to 1.1 V. **e**, Pt L_{III}-edge EXAFS spectra recorded at representative potentials ascending from 0.42 V, 0.8 V to 1.1 V. **f**, differential Δμ XANES spectra at Pt L_{III} edge.

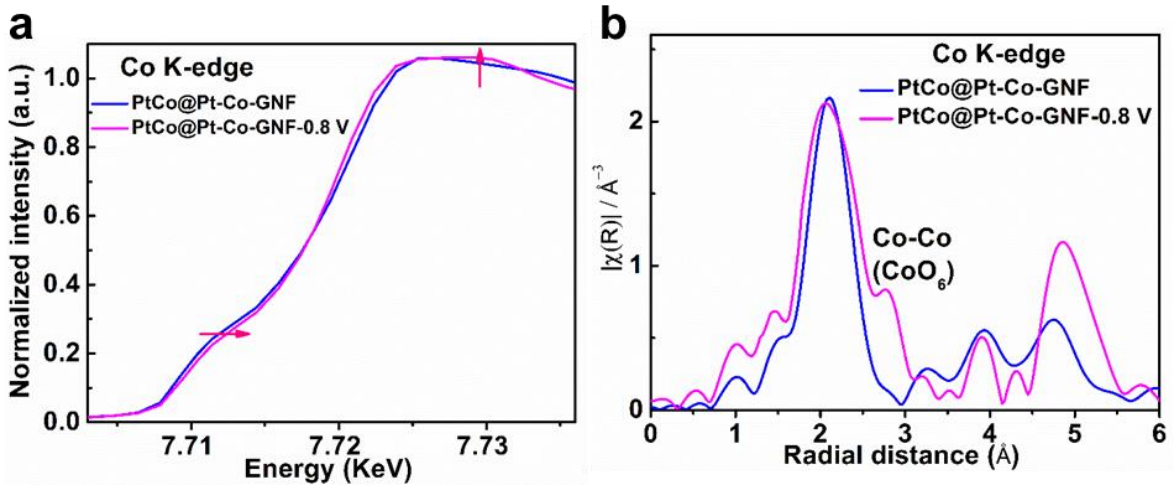

Supplementary Fig. 29 | a, XANES and **b**, EXAFS spectra at Co K-edge for the PtCo@Pt-Co-GNF (ex-situ sample) and PtCo@Pt-Co-GNF -0.8 V in O_2 saturated 0.1 M $HClO_4$ electrolyte (in-situ sample at applied potential of 0.8 V). The EXAFS spectrum at Co K-edge of the in-situ sample is different from that of the ex-situ sample.

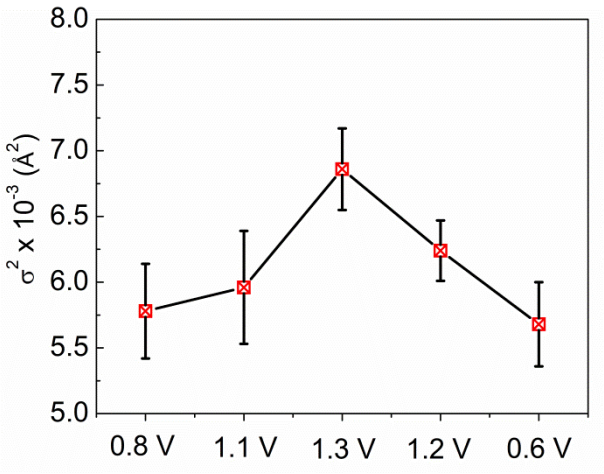

Supplementary Fig. 30 | Debye-Waller factor (σ^2) as function of applied potentials during Operando XAS measurements for PtCo@Pt-Co-GNF in O_2 saturated 0.1 M $HClO_4$ electrolyte.

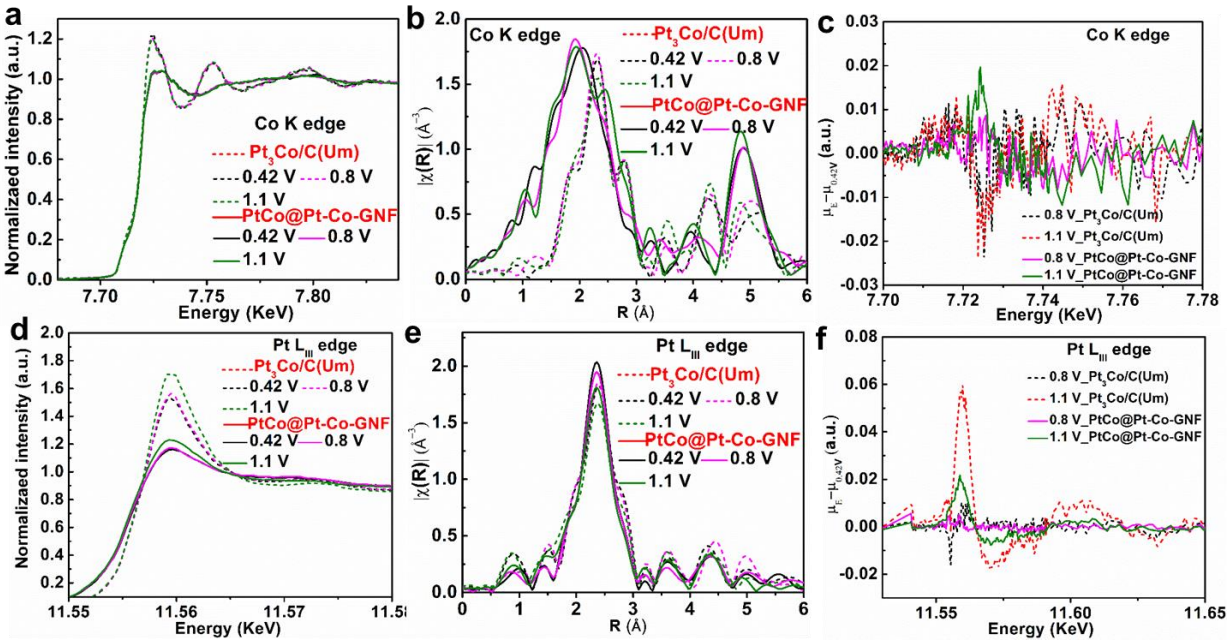

Supplementary Fig. 31 | a, XANES spectra at Co K-edge recorded at representative potentials of 0.42 V, 0.8 V and 1.1 V in Ar saturated 0.1 M $HClO_4$ electrolyte for sample PtCo@Pt-Co-GNF and compared to that for Pt_3Co/C(Um). **b**, EXAFS spectra at Co K-edge recorded at representative potentials of 0.42 V, 0.8 V and 1.1 V in Ar saturated 0.1 M $HClO_4$ electrolyte for sample PtCo@Pt-Co-GNF and compared to that for Pt_3Co/C(Um). **c**, differential Δμ XANES spectra at Co K edge for sample PtCo@Pt-Co-GNF and compared to that for Pt_3Co/C(Um). **d**, XANES spectra at Pt L_{III}-edge recorded at representative potentials of 0.42 V, 0.8 V and 1.1 V in Ar saturated 0.1 M $HClO_4$ electrolyte for sample PtCo@Pt-Co-GNF and compared to that for Pt_3Co/C(Um). **e**, EXAFS spectra at Pt L_{III}-edge recorded at representative potentials of 0.42 V, 0.8 V and 1.1 V in Ar saturated 0.1 M $HClO_4$ electrolyte for sample PtCo@Pt-Co-GNF and compared to that for Pt_3Co/C(Um). **f**, differential Δμ XANES spectra at Pt L_{III} edge for sample PtCo@Pt-Co-GNF and compared to that for Pt_3Co/C(Um).

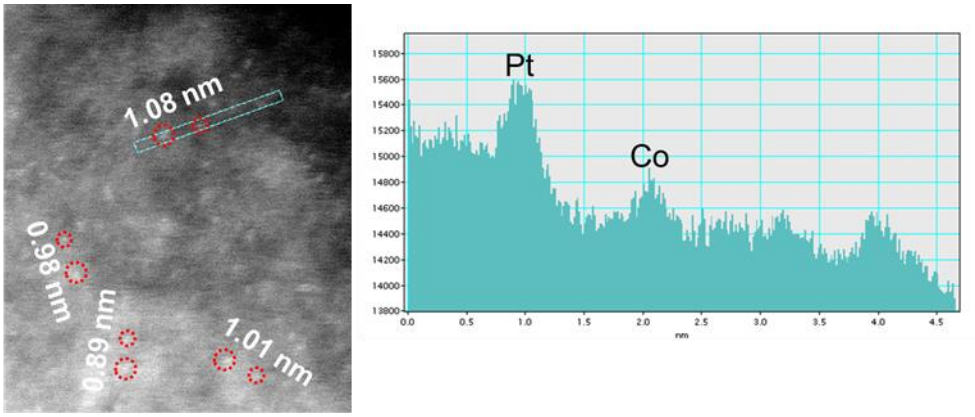

Supplementary Fig. 32 | ACAT-STEM image of the substrate showing the distance between single atomic Pt and Co.

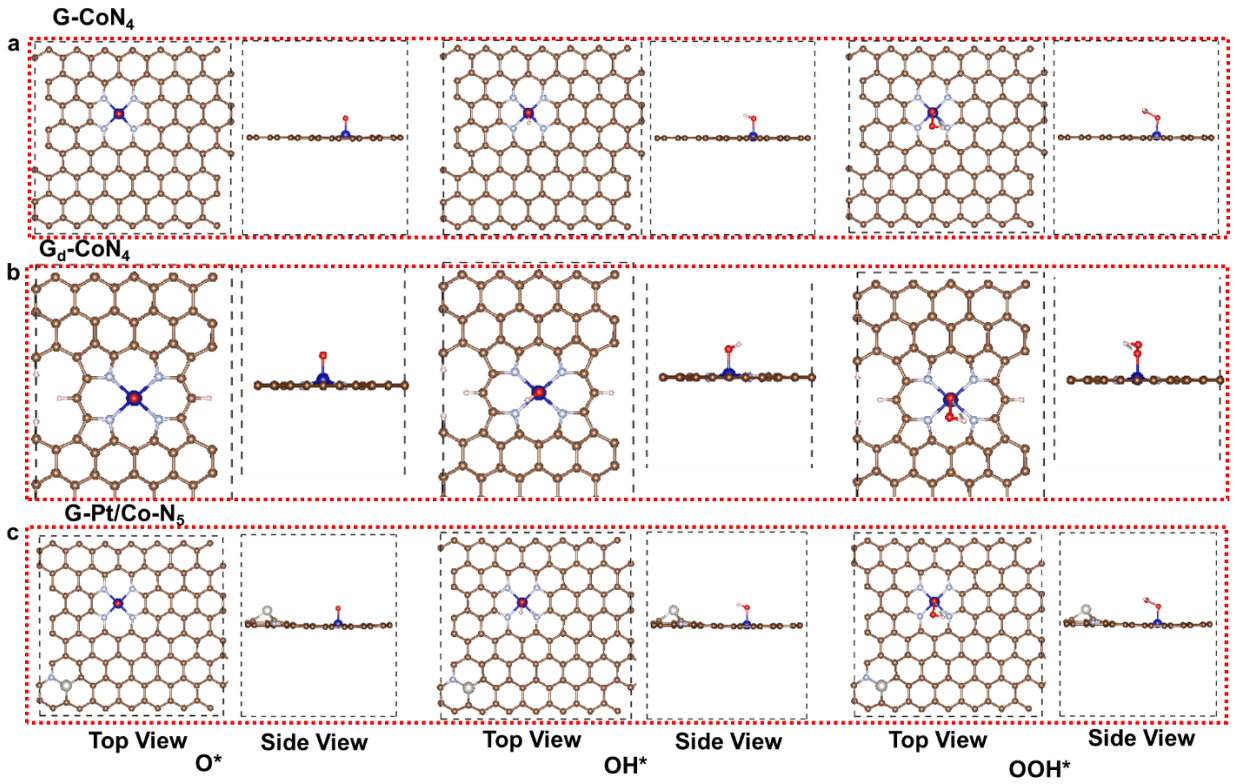

Supplementary Fig. 33 | Optimized atomic configurations of oxygen intermediates (O*, OH* and OOH*) absorbed on Co-N_4 (G-CoN_4, **a**), Co-N_4 at the edge of graphene (G_d-CoN_4, **b**), and Co-N_4 in G-Pt/Co-N_5 (**c**). The most energetically favorable distance between atomic Pt and Co is calculated to be ~ 1 nm, consistent with the experimental result shown in the TEM image (Supplementary Fig. 32).

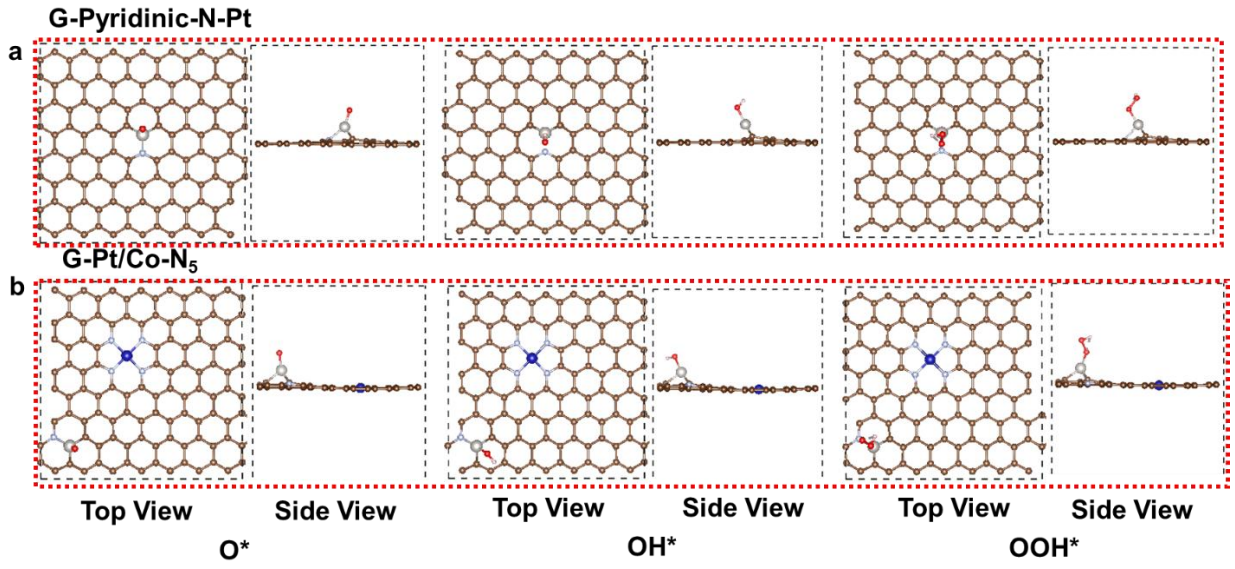

Supplementary Fig. 34 | Optimized atomic configurations of oxygen intermediates (O*, OH* and OOH*) absorbed on Pt-N in G-Pyridinic-N-Pt, **a**, and Pt-N in G-Pt/Co-N_5, **b**.

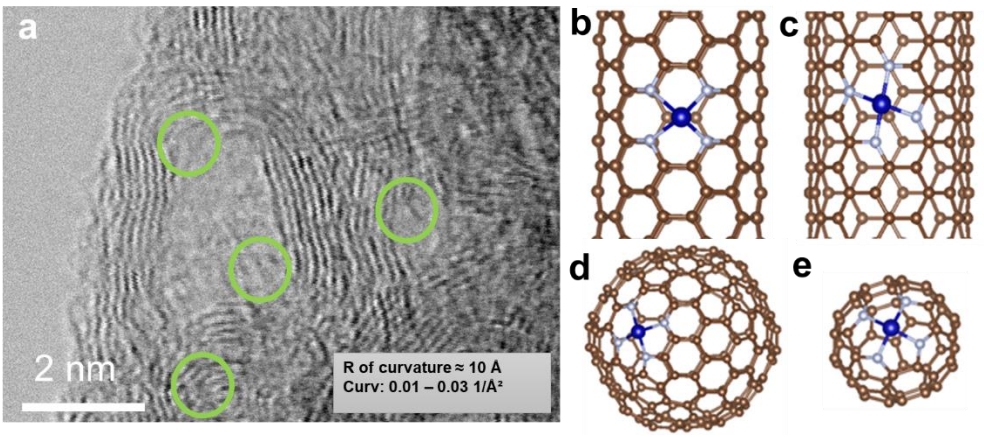

Supplementary Fig. 35 |a, HRTEM image of the fibrous carbon substrate in PtCo@Pt-Co-GNF, the green cycle indicates the curvature contributor; **b-e**, Schematic structure of the proposed Co-N_4 decorated carbon nanotube and nanosphere in the DFT simulation for curvature effect. (Legend: brawn = C, white = N, blue = Co). **b**, (6, 6) nanotube with a symmetric Co-N_4 site; **c**, (6, 6) the same nanotube with an asymmetric Co-N_4 site; **d**, C_{180} carbon sphere; **e**, C_{60} (buckyball).

When we add the Co-N_4 group to the nanotube, there are two ways to create the structure, due to the change of symmetry of the structure. We label these two sites either S1 or S2, with S2 corresponding to a structure where there is no planar symmetry in the site, while S1 maintains symmetry. Examples of S1 and S2 sites were shown in Supplementary Fig. 35.

Finding the ground state for these carbon nanotube structures was a multi-step process. First, to converge these structures, we strained and stressed the z dimension of the tube (the length) and converged at each geometry so that we could make a function of state as a function of strain to find the min value for each nanotube. The rationale is that dimensions along the length of the tube can change in order to relieve stress being in this configuration. This change of length was only significant for the tubes with radii less than 2 Å. We found that when the diameter of the tube surpassed roughly 9 Å, there was no need to further perform this test as the minimum was virtually zero, meaning that the average bond lengths stayed the same as it did in the graphene case. Following this process, the most stable carbon nanotube based on the equation of state at each radius had six carbon atoms removed, and when the Co-N_4 group was added, the structure was relaxed as usual to find an approximate ground-state energy. Once the initial structure was obtained, the various adsorbate binding configurations were performed as well to get an initial geometry. If these energies were used as it is, however, there was no real insight as for the energies between the structures varied extensively. We observed that the final spin states for the structures were all over the place and this caused binding

energies to change by as much as 1.5 eV. Thus, we need to find the ground state magnetic configuration as well, which is a common problem we have observed for 3-d metals. To do this, we fixed the spin for each structure (both with and without adsorbate), ranging from 0 to 6. It should be noted that for a given structure, either the set of odd or even spins were used, as a spin transition of 1 is forbidden. Whether the odd or even set was utilized depends on the number of electrons in the system. The system was then allowed to relax and reach the ground state energy for each of the fixed spin states, along with additionally computing the charge density. In the present work, we observed drastically lower energies for specific spin states for a set of data that consisted of the same transition metal center and the adsorbate. We further performed one more set of relaxations. Removing the spin constraints and starting from previously calculated charge density with fixed spin would ideally allow us to reach a non-integer spin state if it existed. This was done on a twenty-structure subset for each spin state, even highly unstable ones, to see if the fixed spin state with the lowest energy would converge to the minimum energy structure. As we found this to work, only the structure with lowest energy fixed spin state was rerun. In some cases, the final magnetic moment increased while decreased in others.

Ideally, one could calculate a two-point curvature. However, for the traditional formula for curvature, we would just expect to see 1/r for a nanotube. We then tried looking at multiple equations that treated the two curvatures independently; the sum of the computed structures and curvatures were listed in Supplementary Table 7. Thus, we concluded that there must be some coupling term.

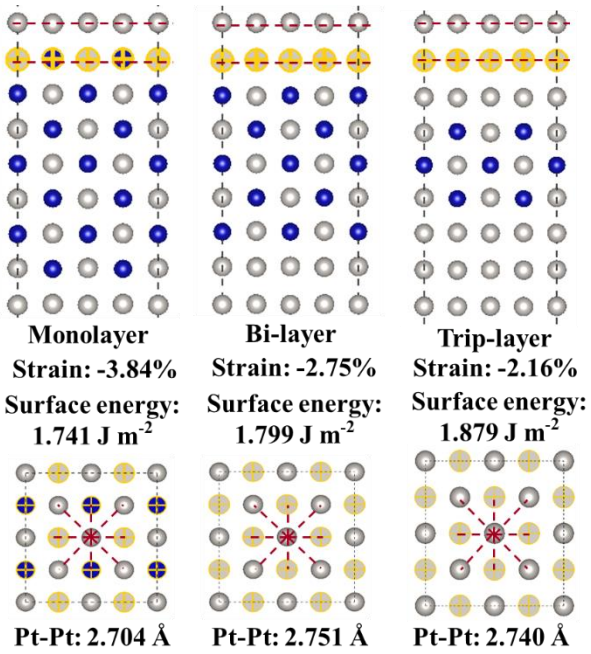

Supplementary Fig. 36 | The structure of PtCo NP with different Pt layers, showing the lowest surface energy and the largest strain for PtCo NP with monolayer Pt which indicates the domination of the PtCo@mono-layer Pt, in line with we observed experimentally.

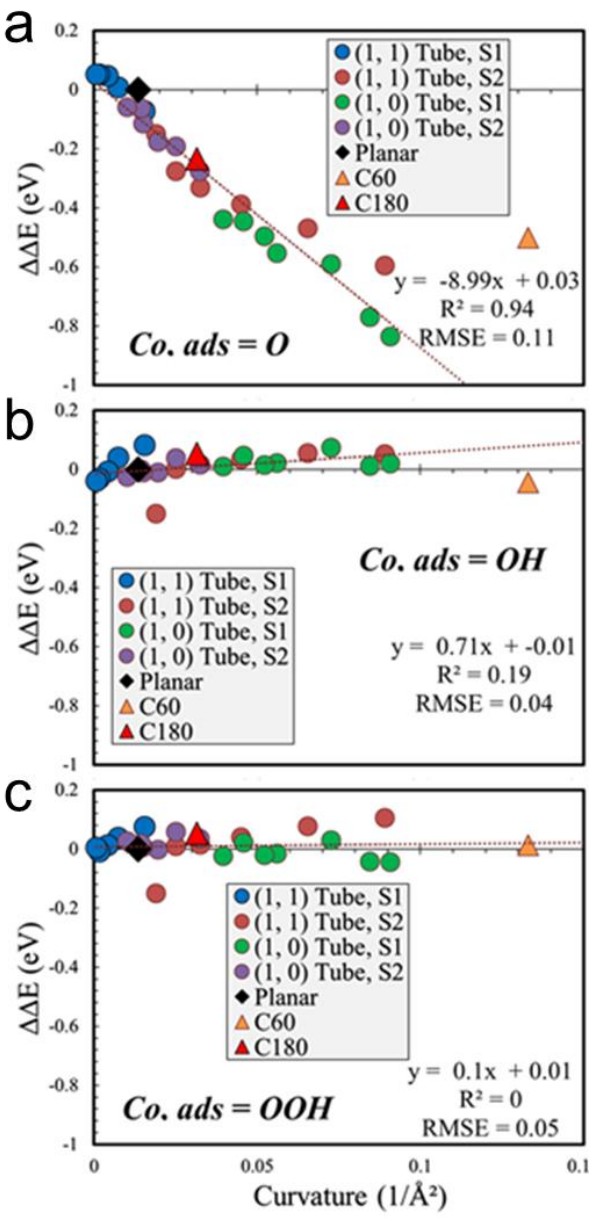

Supplementary Fig. 37 | Changes in binding energy of the O* **a**, OH* **b,** and OOH* **c**, respectively, to Co-N_4 active sites as function of the effective curvature for multiple structures. OH* and OOH* show no appreciable dependence on the curvature, while O* does.

Table S1. Specific surface area analysis of Co-N-GF and PtCo@Pt-Co-GNF.

Sample	S_{BET}/ m^2 g^{-1}	Micropore area / m^2 g^{-1}	External surface / m^2 g^{-1}	Average pore size / nm
Co-N-GF	824.7	308.0	516.7	7.3
PtCo@Pt-Co-GNF	701.4	323.2	378.2	8.0

Table S2. BET surface areas and pore volume distribution of Co-N-GF obtained from different Co-MOF content in the Co-MOF/PAN fiber precursors, which were pyrolyzed at 1000 ºC for 1.5 h in flowing Ar.

CoMOF content	BET Surface Area ($m^2\ g^{-1}$)	$V_{Micropore}$ ($cm^3\ g^{-1}$)	$V_{Mesopore}$ ($cm^3\ g^{-1}$)	$V_{Macropore}$ ($cm^3\ g^{-1}$)
10 wt.%	393.3	0.11	0.24	0.27
20 wt.%	629.4	0.17	0.35	0.25
36 wt.%	824.7	0.53	0.19	0.13
100 wt.%	698.3	0.25	0.28	0.21

Table S3. BET surface areas and pore volume distribution of Co-N-GF obtained from 36% Co-MOF content in the Co-MOF/PAN fiber precursor followed by pyrolysis in flowing Ar at 1000 °C for various times periods.

Time of pyrolysis	BET Surface Area ($m^2\ g^{-1}$)	$V_{Micropore}$ ($cm^3\ g^{-1}$)	$V_{Mesopore}$ ($cm^3\ g^{-1}$)	$V_{Macropore}$ ($cm^3\ g^{-1}$)	Co wt.%
1 h	614.7	0.28	0.32	0.24	9 ~ 11
1.5 h	824.7	0.53	0.19	0.13	6 ~ 8
2 h	1200.0	0.33	0.17	0.6	10 ~ 12

Table S4. Comparisons of ORR performance of PtCo@Pt-Co-GNF with recently reported Pt-based catalysts both in RDE and operating fuel cell.

Catalyst	RRDE						PEM Fuel cell					Ref.
	MA ($A\ mg_{Pt}^{-1}$)	SA ($mA\ cm^{-2}$)	ECSA ($m^2\ g_{Pt}^{-1}$)	Durability loss in MA(%)	Anode Pt loadings ($mg\ cm^{-2}$)	Cathode Pt loadings ($mg\ cm^{-2}$)	MA@0.9V BOL($A\ cm^{-2}$)	MA@0.9V EOL($A\ cm^{-2}$)	Voltage loss at 0.8 $A\ cm^{-2}$ (mV)	Current at 0.8V(H_2-Air cell) ($mA\ cm^{-2}$)	Pt utilization 150 KPa($kW\ g_{Pt}^{-1}$)	
PtCo@Pt-Co-GNF	**5.48 ± 0.41**	**22.2**	**226**	**10 K, 14%**	**0.035**	**0.048**	**2.48 ± 0.18**	**1.98 ± 0.16**	**0**	**438**	**11.9 ± 0.8 (80 °C)**	**This work**
DOE					**Total 0.125**		**0.44**	**0.26 (≤ 40%)**	**≤ 30**	**≥300**	**8**	**4**
PtCo/HSC-f					0.025	0.06	0.7	TBD	TBD	382	10.6 (94 °C)	5
PtCo/HSC-e					0.025	0.1	0.6	40% in loss	20	306	7.1 (94 °C)	5
Pt@CS@CNF900	0.1167[a]		178[a]		0.1	0.125	NA	NA	+1%	NA	NA	6
PtNiCo NWs	4.20	5.11	82.2	30k, 21.4%	0.05	0.1						7
Pt-Ni NPs					0.05	0.1	0.62	0.56	~ 30	125		8
Pt/N-KB 900°C					~0.15	~0.11	0.202	0.199		~250		9
LP@PF-2	12.36		150		0.35	0.043	1.87	0.266				10
LP@PF-2					0.35		1.1	0.98				10
L10-CoPt/Pt	2.26	8.26	27.3		0.105	0.105	0.56	0.45	~ 20	~ 280		11
PtNi-BNCs	3.52	5.16	68.2	50K, 1.1%	0.1	0.15	NA	NA				12
Jagged Pt NW	13.6	11.5	118	10K, 12%								13
PtPb/Pt plate	4.3	7.8	55.1	50k, 7.7%								14
Pt–CoO heat	8.37 ± 0.55	5.38 ± 0.21	156 ± 4									15
PtPb/PtNi IM	1.92	5.16	37.2	10K,17.2%								16
Pt_3Fe NW	2.11	4.34	34.0	50K,24.6%								17

Table S5. EXAFS simulation parameters at Co K edge and Pt L_{III} edge of PtCo@Pt-Co-GNF (ex-situ). k = 2.5 - 12.5 $Å^{-1}$.

Catalyst	Shell	CN	R (Å)	σ^2 ($Å^2$)	R -factor
Co K-edge	Co-Co metal	10.8 ± 0.6	2.528 ± 0.008	0.010 ± 0.001	0.0095
	Co-Pt alloy	6.8 ± 0.5	2.651 ± 0.003		
	Co-N	3.3 ± 0.3	1.930 ± 0.004		
Pt L_{III}-edge	Pt-Co alloy	6.8 ± 0.5	2.627 ± 0.002	0.007 ± 0.001	0.0093
	Pt-Pt alloy	4.0 ± 0.3	2.664 ± 0.002		
model	Co-N	4	1.915		
	Co-Co metal	12	2.524		
	Pt-Co alloy	8	2.646		
	Pt-Pt alloy	4	2.683		

Table S6. Pt L_{III} edge EXAFS simulation parameters of PtCo@Pt-Co-GNF in O_2 saturated 0.1 M $HClO_4$ electrolyte at different applied potentials. k = 2.5 - 12.0 $Å^{-1}$, R = 1.5 - 3.2 Å.

Sample	Shell	CN	R (Å)	σ^2 x 10^{-3} ($Å^2$)	R-factor
0.8 V	Pt-Co	6.8 ± 0.2	2.65 ± 0.01	5.78 ± 0.36	0.006
	Pt-Pt	4.0 ± 0.2	2.69 ± 0.02		
1.1 V	Pt-Co	6.9 ± 0.2	2.64 ± 0.02	5.96 ± 0.43	0.009
	Pt-Pt	4.0 ± 0.1	2.68 ± 0.01		
1.3 V	Pt-Co	7.0 ± 0.4	2.64 ± 0.03	6.86 ± 0.31	0.010
	Pt-Pt	4.0 ± 0.1	2.68 ± 0.01		
1.2 V	Pt-Co	7.0 ± 0.3	2.65 ± 0.03	6.24 ± 0.23	0.010
	Pt-Pt	4.0 ± 0.1	2.69 ± 0.02		
0.6 V	Pt-Co	7.0 ± 0.3	2.65 ± 0.02	5.68 ± 0.32	0.008
	Pt-Pt	4.0 ± 0.1	2.69 ± 0.03		

Table S7. List of all nanotube structures and the corresponding curvatures that were computed.

Nanotube	n	symmetry	nanotube radius (Å)	R1 (Å)	R2 (Å)	κ (1/Å²)
(n,n)	3	symmetric	2.1	7.8	7.8	0.049
(n,n)	4	symmetric	2.8	14.1	14.1	0.015
(n,n)	5	symmetric	3.4	20.3	20.6	0.007
(n,n)	6	symmetric	4.1	27.1	27.2	0.004
(n,n)	7	symmetric	4.8	46	40.3	0.002
(n,n)	8	symmetric	5.4	66.2	64.4	0.001
(n,n)	9	symmetric	6.1	103.5	97	0.000
(n,n)	3	non-symmetric	2.1	2.5	39.1	0.171
(n,n)	4	non-symmetric	2.8	793.7	3.4	0.087
(n,n)	5	non-symmetric	3.4	151.7	4	0.064
(n,n)	6	non-symmetric	4.1	4.8	248.4	0.044
(n,n)	7	non-symmetric	4.8	346.3	5.6	0.032
(n,n)	8	non-symmetric	5.4	500.9	6.4	0.025
(n,n)	9	non-symmetric	6.1	692.6	7.3	0.019
(n,0)	6	symmetric	2.4	5.1	6.2	0.096
(n,0)	7	symmetric	2.8	6.3	5.4	0.089
(n,0)	8	symmetric	3.2	6.2	5.9	0.082
(n,0)	9	symmetric	3.6	6.4	6.6	0.071
(n,0)	10	symmetric	4	7.1	7.7	0.055
(n,0)	11	symmetric	4.4	7.7	7.7	0.051
(n,0)	12	symmetric	4.7	8.2	8.2	0.045
(n,0)	13	symmetric	5.1	8.9	8.7	0.039
(n,0)	6	non-symmetric	2.4	4.2	110.4	0.059
(n,0)	7	non-symmetric	2.8	5	112.3	0.042
(n,0)	8	non-symmetric	3.2	5.6	395.3	0.032
(n,0)	9	non-symmetric	3.6	6.4	345.9	0.025
(n,0)	10	non-symmetric	4	7.2	528.9	0.020
(n,0)	11	non-symmetric	4.4	8.2	721.9	0.015
(n,0)	12	non-symmetric	4.7	8.8	88.2	0.014
(n,0)	13	non-symmetric	5.1	10	1082.2	0.010

Table S8 Work of adhesion between PtCo NP and the graphene substrate with / without Co-N-G.

System	eV
Interface	Work of adhesion
PtCo/G	-3.905242637
PtCo/Co-N-G	-4.097287567

Supplementary References

1 Jaouen Fdr., Lefe`vre M., Dodelet J. -P., Cai M., Heat-treated Fe/N/C catalysts for O_2 electroreduction: Are active sites hosted in micropores? *J. Phys. Chem. B.* **110**, 5553-5558 (2006).

2 Jaouen Fdr., *et al.* Cross-laboratory experimental study of non-noble-metal electrocatalysts for the oxygen reduction reaction. *ACS Appl. Mater. Interfaces* **1**, 1623-1639 (2009).

3 Gloaguen F., Leger J. -M., Lamy C., Electrocatalytic Oxidation of Methanol on Platinum Nanoparticles Electrodeposited onto Porous Carbon Substrates. *J. Appl. Electrochem.* **27**, 1052-1060 (1997).

4 DOE FCTTR. US DRIVE Partnership. Fuel Cell Technical Team Roadmap, November 2017, https://www.energy.gov/sites/prod/files/2017/11/f46/FCTT_Roadmap_Nov_2017_FINAL.pdf. (2017).

5 Kongkanand A., Annual Merit Review DOE Hydrogen and Fuel Cells and Vehicle Technologies Programs, Washington, DC, 2018, https://www.hydrogen.energy.gov/pdfs/review18/fc144_kongkanand_2018_o.pdf.

6 Karuppannan M., *et al.* A highly durable carbon-nanofiber-supported Pt–C core–shell cathode catalyst for ultra-low Pt loading proton exchange membrane fuel cells: facile carbon encapsulation. *Energy. Environ. Sci.* **12**, 2820-2829 (2019).

7. Jiang K., *et al.* Efficient oxygen reduction catalysis by subnanometer Pt alloy nanowires. *Sci. Adv.* **3**, 1601705 (2017).

8. Han B., *et al.* Record activity and stability of dealloyed bimetallic catalysts for proton exchange membrane fuel cells. *Energy. Environ. Sci.* **8**, 258-266 (2015).

9. Ott S., *et al.* Ionomer distribution control in porous carbon-supported catalyst layers for high-power and low Pt-loaded proton exchange membrane fuel cells. *Nat. Mater.* **19**, 77-85 (2020).

10. Chong L., *et al.* Ultralow-loading platinum-cobalt fuel cell catalysts derived from imidazolate frameworks. *Science* **362**, 1276-1281 (2018).

11. Li J., *et al.* Hard-Magnet L_{10}-CoPt Nanoparticles Advance Fuel Cell Catalysis. *Joule* **3**, 124-135 (2019).

12. Tian X., *et al.* Engineering bunched Pt-Ni alloy nanocages for efficient oxygen reduction in practical fuel cells. *Science* **366**, 850-856 (2019).

13. Li M., *et al.* Ultrafine jagged platinum nanowires enable ultrahigh mass activity for the oxygen reduction reaction. *Science* **354**, 1414-1419 (2016).

14. Bu L., *et al.* Biaxially strained PtPb/Pt core/shell nanoplate boosts oxygen reduction catalysis. *Science* **354**, 1410-1414 (2016).

15. Sievers G. W., *et al.* Self-supported Pt-CoO networks combining high specific activity with high surface area for oxygen reduction. *Nat. Mater.* **20**, 208-213 (2020).

16. Bu L., *et al.* PtPb/PtNi Intermetallic Core/Atomic Layer Shell Octahedra for Efficient Oxygen Reduction Electrocatalysis. *J. Am. Chem. Soc*. **139**, 9576-9582 (2017).

17. Luo M., *et al.* Stable High-Index Faceted Pt Skin on Zigzag-Like PtFe Nanowires Enhances Oxygen Reduction Catalysis. *Adv. Mater*. **30**, 1705515 (2018).